Coupled Non-Conforming Finite Element and Finite Difference Approximation Based on Laminate Extrapolation to Simulate Liquid Composite Molding Processes. Part I: Isothermal Flow

Edu Ruiz*, V. Achim and F. Trochu

Centre de Recherches Appliquées Sur les Polymères (CRASP), Département de Génie Mécanique, École Polytechnique de l'Universite de Montréal, H3C 3A7, Canada

ABSTRACT

In composite manufacturing by resin injection through a fibrous reinforcement, several phenomena occur involving the flow of resin and heat exchanges by the resin with the fiber bed and the mold. During processing, through-thickness flows commonly appear when the fibrous preform is made out of a stack of plies of different permeabilities. In many situations, simulation of the mold filling in Liquid Composite Molding (LCM) requires performance of a full three-dimensional analysis. In the pre-processing stage, the construction of three-dimensional finite element meshes of complex parts made out of components of small thickness with respect to their length is very tedious. These parts are typically composed of an assembly of shell and flat panels. In such parts, a good aspect ratio of the finite elements must be respected to ensure appropriate simulation results. These conditions result in meshes with a very large number of degrees of freedom, which translates into a too high computational burden. For these reasons, a new numerical approach is presented in this paper for accurate and faster simulation of the filling phase in LCM. Based on the fabric reinforcement layup, a new non-conforming finite element is developed to quickly evaluate the through-thickness flow. Starting with a spatial triangular mesh as input geometry and based on the stacking sequence of the preform, an extrapolation algorithm is used to extrude the mesh in the thickness direction and generate the 3D non-conforming finite elements. To further evaluate the validity of the three-dimensional model, an experimental verification was performed for a typical through-thickness flow. Then, a comparative study is conducted to demonstrate the advantages of the proposed methodology in terms of accuracy. The results are compared with 2D (triangles) and 3D (tetrahedrons) finite element solutions. Finally, the performance of the model is assessed in terms of computer time.

Key Words: Liquid Composite Molding (LCM), composites processing modeling, non-conforming finite element, mesh extrapolation, laminate structure.

INTRODUCTION

Polymer composites are presently the focus of much interest for the engineering design of structural and semi-structural parts. Diverse composite processing techniques have been investigated in recent years to improve part quality and reduce manufacturing costs. In

* e-mail: edu.ruiz@polymtl.ca
Postal address: C.P. 6079, succ. Centre-Ville
Montreal (Quebec) Canada, H3C 3A7
Tel.: Edu Ruiz: (514) 340-4711 ext. 4585; Fax: (514) 340-5867

the processing of thermosetting polymer matrices, Liquid Composite Molding (LCM) techniques such as Resin Transfer Molding (RTM) or Resin Film Infusion (RFI) have demonstrated potential advantages over traditional methods. In the aerospace field, the RTM process has now become mature technology to manufacture high performance composites by resin injection. In the automobile sector, these technologies are still expensive and present research aims mainly at reducing cycle time. Several automotive companies have recently launched investigations or collaborate in research networks such as Auto 21 /1/ to acquire advanced knowledge on these new manufacturing techniques and improve the design of production tools. Appropriate tooling is actually crucial to ensure proper mold filling and curing of composite parts. Air bubbles, dry spots or resin rich areas are common problems that must be avoided during the filling stage. Residual stresses, warpage and spring-in are another category of problems that occur during processing. In these comprehensive investigations, numerical simulation is critical to successfully design the mold and optimize the production cycle.

The advantage of computational techniques to prevent filling problems and get better molding results was established by several authors /2-6/. Analysis of mold deformation during filling /3/, comparison of various injection strategies and optimization of the injection flow rate /6/ illustrate the potential advantages brought by numerical simulation. Even if these advantages have been well defined, filling simulations are mainly carried out in thin shell geometries for the following reasons: (1) composite parts have usually a small thickness compared to their surfaces so that usually the through-thickness flow can be neglected; (2) the generation of a 3D mesh for a part of small thickness is a complex operation. The setup of boundary conditions is not an easy task for complex 3D parts; (3) the number of solid finite elements required to obtain accurate solutions makes three-dimensional simulation tedious in terms of computer time.

In this paper, a new methodology is proposed to compute complex flows in LCM. The method is based on the concept of non-conforming finite element and mesh extrusion. Starting with a mid-surface mesh, a three-dimensional mesh is constructed by extrusion from the two-dimensional finite element mesh. The extrusion is defined by the preform stacking sequence. Different fabric permeabilities and fiber volume fractions can be used in each laminate ply. After starting the computations that govern fluid flows through porous media, the discretized finite element (FE) formulation is developed with the non-conforming shape functions defined on prismatic elements. To evaluate the validity of the calculations, the results of two experiments are compared to the numerical solution: (1) unidirectional flow through a multi-layer preform; (2) pointwise injection in a thick part. Finally, the test case of a truck fender is studied to assess the quality of the proposed methodology and compare the results of three-dimensional flow simulations with two-dimensional calculations.

GOVERNING EQUATIONS

A typical mold filling process to manufacture composite parts involves the injection of a liquid resin into the mold cavity. As illustrated in Figure 1, the central issue in the analysis of mold filling consists of tracking the free surface between the filling material (i.e. liquid resin) and the escaping gas (usually air) present in the mold cavity before the injection. The flow of fluid through a fibrous network has been analyzed either at the microscopic or macroscopic levels. In the microscopic analysis, the flow through the fibrous reinforcement is governed by Navier-Stokes equation. However, this approach may be misleading because of the complex architecture of the reinforcement and the difficulty to find appropriate boundary conditions. In macroscopic investigations, the flow of resin through a fiber bed is modeled by Darcy's law, which governs incompressible flows through porous media. Therefore the filling stage in LCM must respect resin mass conservation and following Darcy's law, the resin flow rate is proportional to the pressure drop.

A porous medium may be defined as a solid containing holes or voids, connected or not, regularly or randomly dispersed. Porosity is the fraction of the bulk volume of the material occupied by voids. Permeability

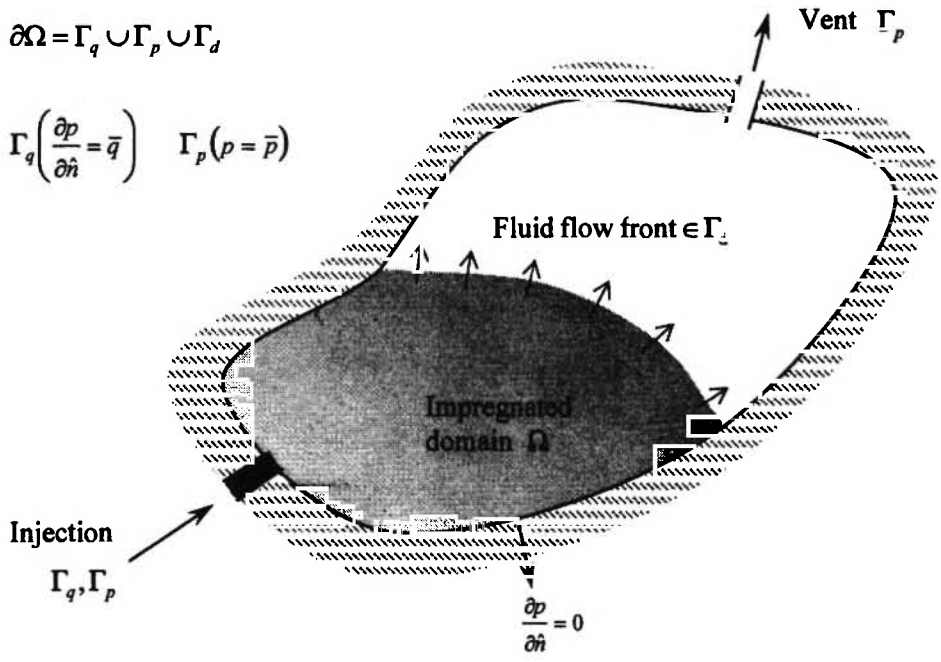

Fig. 1: Schematic representation of the domain Ω representing the mold cavity. The boundary is defined by $\partial\Omega = \Gamma_q \cup \Gamma_p \cup \Gamma_d$. (Note that Γ_d was deliberately removed for clarity.)

is the property that characterizes the facility of a fluid submitted to a pressure field to permeate through a porous medium. In order to simulate the filling process, several assumptions must be made to simplify the problem. In general, the fabric reinforcement placed in the mold cavity is assumed to be rigid during filling and inertia effects are neglected because of the low Reynolds number. Furthermore, at the pressure level usually created in LCM molds to drive the flow, surface tension may be neglected compared to the dominant viscous force. The equation of mass conservation for the fluid phase can then be written as:

$$div(\rho.\bar{v}) = 0 \tag{1}$$

where ρ is the density of the resin injected and $\bar{v}$ is the fluid velocity, i.e. the velocity at which the fluid actually travels, rather than the observed macroscopic velocity. Note that we consider here that the flow takes place in rigid molds. Otherwise the equation of mass conservation (1) should consider also deformation of the fabric structure. Darcy's law is as the equation that drives the flow of an incompressible fluid through a porous medium. It is expressed as follows:

$$\bar{v} = -\frac{1}{\mu}[K].\nabla p \tag{2}$$

where $[K]$ is a 3x3 permeability tensor, μ is the resin viscosity and ∇p is the pressure gradient. Equation (2) relates the three components of the superficial fluid velocity vector to the pressure. This relationship is only valid for Newtonian fluids and ignores gravity effects and mold deformation. Note that these effects can also be considered using a more elaborate equation /7/. Combining equations (1) and (2), the partial differential equation that governs the fluid flow is:

$$div\left(-\frac{1}{\mu}[K].\nabla p\right) = -\varphi \tag{3}$$

where p is the scalar potential on Ω (see Figure 1). The term $[K]/\mu$ represents the dual scalar field and φ is a volume source term.

Potential formulation

To solve equations (1) and (2), a weak formulation can be written in terms of weighted residuals /8/. Defining a test function equal to the scalar potential p and introducing a space $F(\Omega)$ of shape functions w, the elliptic partial differential equation (3) is replaced by an equivalent variational or weak formulation obtained as the integral of the scalar potential p on Ω multiplied by w. The weak formulation can be expressed as follows:

$$\int_{\Omega} w \cdot div\left(-\frac{1}{\mu}[K].\nabla p\right)\partial\Omega + \int_{\Omega}(w\cdot\varphi)\partial\Omega = 0 \qquad (4)$$

for any *test function* w belonging to the space $F(\Omega)$. If Green's theorem is applied for a Newtonian and incompressible fluid without any source term, the integration by parts gives:

$$\int_{\Omega}\nabla w\cdot\left(-\frac{1}{\mu}[K].\nabla p\right)\partial\Omega - \int_{\Gamma_d}\left(w\cdot(\hat{n}\cdot\bar{v})\right)\partial\Gamma_d = 0,$$
$$\forall w \in F(\Omega) \qquad (5)$$

FINITE ELEMENTS DISCRETIZATION

The discrete finite element method (FEM) consists of finding a set of shape functions w that properly approximate the scalar potential p on the whole domain Ω. The scalar potential is unknown in Ω, but defined on the boundaries Γ_q, Γ_p and on the flow front. The domain Ω is decomposed into small elements of simple geometrical shape, where p is approximated by a linear combination of *shape functions* defined on a specific finite element of the mesh. For a general *shape function* s_n and *test function* s_j associated to the group of nodes in the finite volume V_e, the Galerkin formulation is:

$$\sum_{n=1}^{N_e}\left[p_n\int_{V_e}-\nabla s_j\cdot\left(\frac{[K]}{\mu}\nabla s_n\right)\partial V_e\right] = \int_{\Gamma_e}\left(s_j\cdot(\hat{n}\cdot\bar{v})\right)\partial\Gamma_e,$$
$$\forall s_j \in V_e \qquad (6)$$

where N_e are the element nodes and Γ_e the boundary of the finite volume V_e. The scalar potential field p is computed as

$$p(x) = \sum_{n=1}^{N} p_n s_n(x) \qquad (7)$$

where $s_n(x)$ is a piecewise linear shape function and x the position vector in the domain Ω. In matrix notation, equation (6) can be rewritten as follows:

$$[M]\{p\} = \{R\} \qquad (8)$$

where $[M]$ represents the NxN stiffness matrix of the scalar potential field. An element of matrix M is defined as:

$$a_{jn} = \int_{V_e}\nabla s_j\cdot\left(\frac{[K]}{\mu}\nabla s_n\right)\partial V_e,$$
$$\text{for } j,n = 1,...,N \qquad (9)$$

and $\{R\}$ is a vector $\{r_j\}$ containing the boundary conditions:

$$r_j = \int_{\Gamma_e}\left(s_j\cdot(\hat{n}\cdot\bar{v})\right)\partial\Gamma_e,$$
$$j = 1,...,N \qquad (10)$$

The approximate solution of the scalar potential p is then obtained by solving the linear system (8) of N equations with N unknowns.

Mass conservation and div-conform approximation

In the finite elements discretization of incompressible flows through porous media, the fluid mass is typically assumed to be constant within a defined control volume (CV). In our case, instead of the traditional nodal control volume technique, the geometry of the finite element is considered to represent the control volume where the mass balance equation is solved /2/. The fluid mass transported between adjacent elements is the scalar product of the normal vector with length of the edge at the interface by the mass velocity $\rho\cdot\bar{v}$ (see Figure 2a). The conservation of the fluid

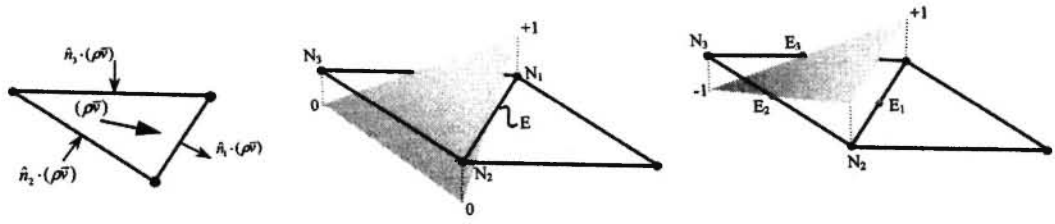

Fig. 2: Triangular finite element: (a) incoming and out-coming flows in the FE; (b) conforming shape function at node N_1; (c) non-conforming shape function associated to edge E_1.

mass at the interface between two adjacent elements is not ensured with *conforming* finite element approximations. As matter of fact, the continuous shape function obtained by Lagrange interpolation at the element nodes (see Figure 2b) results in a piecewise linear scalar approximation of the pressure field on each finite element of the mesh. The gradient of the scalar potential, i.e. the dual scalar field $\bar{v}$, is constant on each element, but the normal fluid velocity is not continuous across the element interface (edge E in Figure 2b). As a result of this discontinuous normal velocity across the interfaces between neighboring elements, the approximate solution of the flow equation (2) does not satisfy exactly the mass balance equation (1).

A discontinuous shape function may be obtained by interpolating the pressure field on the element edges as depicted in Figure 2c in the 2D case. In the 3D case, the interpolation is performed on the faces of each solid element. This non-conforming interpolation leads to a functional space of shape functions that ensures a continuous mass flow, i.e. $\hat{n} \cdot \rho\bar{v}$ is constant across the interfaces between neighboring elements. On the other hand, equation (3) with source term implies that the integral of the divergence in an element is equal to the balance of resin mass flowing across its boundary BC:

$$\int_{CV} div(\rho\bar{v})dV = \int_{BC} \hat{n} \cdot \rho\bar{v}dA \tag{11}$$

In numerical analysis, this kind of approximation is called div-conform. So, the fluid mass is conserved in the flow and across the interfaces between elements. As demonstrated in /9/, the use of non-conforming finite elements is essential to ensure mass conservation and obtain accurate numerical results in the simulation of injection molding.

Finite elements for LCM simulation

In the particular case of pure Darcy's flow, the discontinuous interpolating polynomial may be chosen as piecewise linear /9/. For the triangular non-conforming finite element of Figure 3, the three degrees of freedom are assigned at the middle points of the element edges. Considering a classical reference triangle with a local linear approximation space of dimension 3, the element shape functions s_e write as follows:

$$s_e = \begin{cases} s_1 = 1 - 2\eta \\ s_2 = 2(\zeta + \eta) - 1 \\ s_3 = 1 - 2\zeta \end{cases} \quad 0 \le \zeta, \eta \le 1 \tag{12}$$

where ζ, η and τ are the local coordinates in a local reference system. The gradients of these shape functions can be written as a 3X3 matrix of the form:

$$\dot{s}_e = \begin{bmatrix} 0 & -2 & 0 \\ 2 & 2 & 0 \\ -2 & 0 & 0 \end{bmatrix} \tag{13}$$

Parts manufactured by LCM usually have a surface dimension much larger than their thickness. For this reason, most composite parts are commonly considered as thin shells and simulated using two-dimensional finite element shell approximation with through-thickness averaging. In many cases, three-dimensional simulations are required to predict accurately the injection time and detect local filling problems. Because

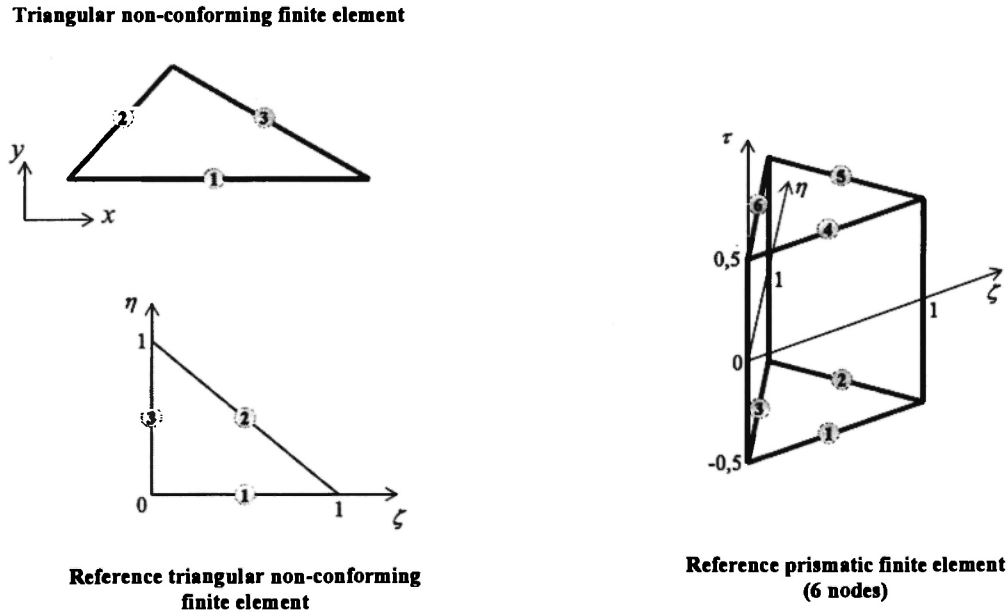

Fig. 3: Triangular and prismatic (6 nodes) non-conforming finite elements. The degrees of freedom are assigned at the middle edges; ζ, η and τ denote the local coordinates in the reference element.

composite parts are made out of thin laminates, parallel layers of three-dimensional finite elements can easily be generated automatically to model the properties of each ply. As will be shown later, prismatic elements constructed from triangular mesh present the advantage of simplifying considerably the mesh generation for composite analysis by allowing parallel processing of layers stacked elements. In this work, a new non-conforming prismatic element is introduced for the three-dimensional analysis of mold filling in LCM. This prismatic element contains 6 nodes and is the result of an extrapolation of a triangular shell element (see Figure 3). The degrees of freedom are also extended on the edges of the two triangular faces. The linear function space will have now 6 degrees of freedom. The element shape functions s_e of the *Prism6* element are:

$$s_e = \begin{cases} s_1 = (1-2\eta)\cdot(1-\tau)\cdot 0{,}5 \\ s_2 = (2\zeta+2\eta-1)\cdot(1-\tau)\cdot 0{,}5 \\ s_3 = (1-2\zeta)\cdot(1-\tau)\cdot 0{,}5 \qquad 0\le\zeta,\eta\le 1 \\ s_4 = (1-2\eta)\cdot(1+\tau)\cdot 0{,}5 \qquad -1\le\tau\le 1 \\ s_5 = (2\zeta+2\eta-1)\cdot(1+\tau)\cdot 0{,}5 \\ s_6 = (1-2\zeta)\cdot(1+\tau)\cdot 0{,}5 \end{cases} \tag{14}$$

where the third dimension τ is referenced from the element midplane. The gradient of the shape function is the following 6x3 matrix:

$$\dot{s}_e = \begin{bmatrix} 0 & -(1-\tau) & -(1-2\eta)\cdot 0{,}5 \\ (1-\tau) & (1-\tau) & -(2\zeta+2\eta-1.)\cdot 0{,}5 \\ -(1-\tau) & 0 & -(1-2\zeta)\cdot 0{,}5 \\ 0 & -(1+\tau) & (1-2\eta)\cdot 0{,}5 \\ (1+\tau) & (1+\tau) & (2\zeta+2\eta-1)\cdot 0{,}5 \\ -(1+\tau) & 0 & (1-2\zeta)\cdot 0{,}5 \end{bmatrix} \tag{15}$$

Note that the *Prism6* element is non-conforming with *div-conformity* in the bottom and top planes of the triangular faces, but it is *div-non conform* through the element thickness. In other words, the resin mass will be conserved in the element plane, but mass may be lost through the element height (or thickness). Because the element thickness in our application is small compared to the part surface, the accuracy of through-thickness flow calculations remained acceptable.

Flow front advancement

The unsteady flow can be solved by considering a succession of quasi steady-state approximations, dividing the problem into a sequence of spatial and transient analyses. At each computed time step, the free surface Γ_d is moving inside the mold cavity Ω. The new location of the free surface is defined by its location at the previous time step and the actual velocity field. The methodology used to track the displacement of the free surface is defined in /9/. A scalar field $S(x,t)$, called the *saturation coefficient* (or fill factor), is defined in Ω. In a fully saturated porous medium (fully impregnated preform) S is equal to one, while in the unsaturated region (dry fabric) it is zero. In the partially saturated medium (in the vicinity of the flow front position), $S(x,t)$ lies between these two values. The fill factor is transported in the partially and fully saturated regions until it finally reaches the value of full saturation (S=1) everywhere in the cavity. The pure transport equation for a scalar field S is:

$$\frac{\partial S}{\partial t} + \bar{v} \cdot \nabla S = 0 \qquad (16)$$

As described in /9/, the control volumes used in this approximation are the finite elements of the mesh. The flow front is then advanced by transporting the fill factor across the inter-element boundaries (the element edges in 2D or the faces in 3D).

APPLICATION TO 3-DIMENSIONAL FLOWS IN LCM

Typical composite parts manufactured by LCM are very often thin shells consisting of planar facets of uniform thickness. The fabric preform is made of homogeneous layers of constant thickness. This implies that the permeability tensor is assumed to have everywhere a symmetry plane parallel to the part midsurface, the in-plane tensor of the component layers is assured not to differ by more than one order of magnitude. This approach allows the isothermal fluid flow to be calculated in two dimensions, in fact in the midplane of the part. The pressure and velocity fields are evaluated by solving the two-dimensional Darcy's equation using a weighted average permeability. The fluid flow is then advanced considering the thickness variations of the part to verify exactly the mass balance in the filling algorithm.

When important variations in the permeability tensor appear between preform layers (or when thickness of the part changes), the fluid will flow with a different velocity in each ply. If the planar velocity strongly differs from one layer to the other, a through-thickness flow is generated across the plies. In this case, the three-dimensional flow solution does not match anymore with the averaged flow, and the approach of a midplane surface is no longer acceptable. In addition, through-thickness phenomena such as dry spots may appear in the low permeability layers, which remain hidden in the averaged flow analysis. In the above cases, three-dimensional solutions must be implemented for accurate prediction of the filling process.

From the experience gained in the simulation of composite processing by LCM, three-dimensional finite element modeling was found to be a complex task that requires advanced knowledge on mesh generation and process parameters. A refined mesh is not always accessible for calculation, and coarse meshes do not provide adequate information on the flow front. Although the midplane surface and 2D mesh can be constructed relatively quickly, the construction of a solid mesh requires a patient work of verification of the lines and surface patches that define the geometry of the part. Once the mesh has been generated, a careful time-consuming check of possible degenerated elements must be performed. In addition, three-dimensional mesh refinement in regions close to flow or thermal boundary conditions is not always evident to achieve (such as remeshing along the edges of a mold cavity to model race-tracking).

MESH GENERATION FOR THROUGH-THICKNESS FLOW ANALYSIS

A potential benefit was found in the concept of mesh extrusion to improve the geometric modeling of 3D parts for LCM simulations. A midplane mesh usually constructed for thin shell simulations, can be extrapolated in a certain number of layers *Nl* (see Figure

4) to create automatically a three-dimensional mesh with a multi-layer structure well suited for composite analysis. Boundary conditions can be easily imposed on any surface of the final mesh. Moreover, the in-plane and through-thickness properties of the fibrous reinforcement can also be set for each extrapolated layer. To extrude the midsurface elements, mesh nodes need first to be extrapolated. To do so, the direction of extrapolation must be defined. As depicted in Figure 5, the node N_i is connected to a group of k two-

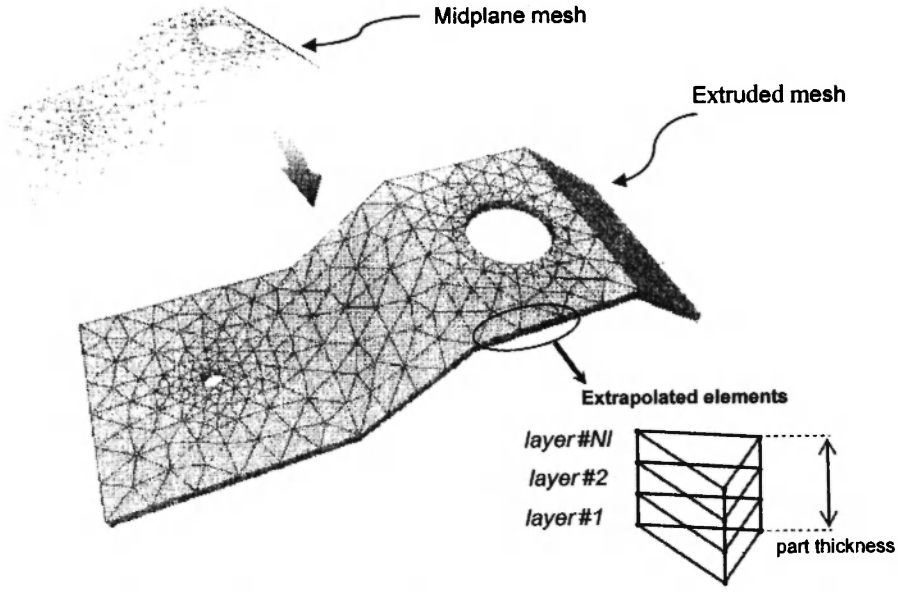

Fig. 4: Extrusion of a midplane mesh through the thickness of the composite. From 2D finite elements, a solid mesh consisting of *Nl* layers may be constructed to calculate 3D flows.

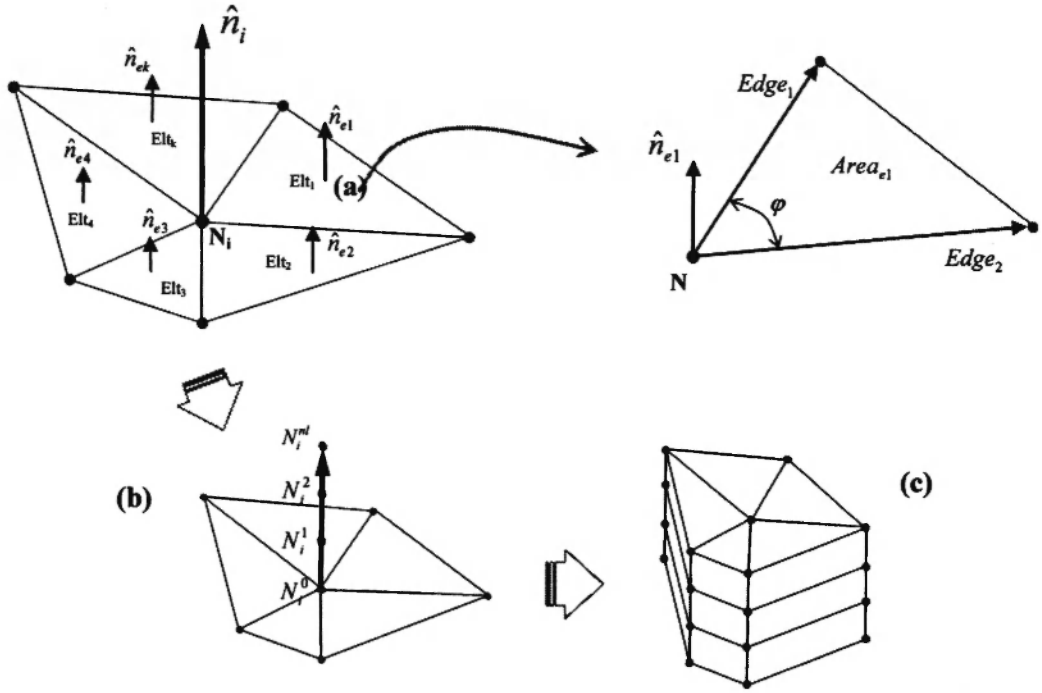

Fig. 5: Procedure for mesh extrusion: (a) the nodes normal are computed from the normals in adjacent elements, (b) new nodes are created along the calculated normal, (c) finally adjacent elements are extruded.

dimensional elements. The normal vector to the discrete geometry at point *Ni* can be evaluated from the normals to the adjacent elements and their aspect ratios. For a typical adjacent element e_1, the normal is interpolated from the vertex normal ($Edge_1$ and $Edge_2$) as follows:

$$\hat{n}_{e_1} = \frac{Edge_1 \times Edge_2}{\|Edge_1 \times Edge_2\|} \tag{17}$$

The extrusion also considers the angles between any two edges of coincident elements that are at the node considered, i.e., the angle defined by:

$$\cos\varphi_{e_1} = \left(\frac{Edge_1 \cdot Edge_2}{\|Edge_1\| \cdot \|Edge_2\|} \right) \tag{18}$$

Let $\hat{n}^{\varphi}_{e_1}$ denote the normal weighted by the base angle φ_{e_1} and $\hat{n}^{A}_{e_1}$ the normal weighted by the area A_{e_1} of element e_1:

$$\hat{n}^{\varphi}_{e_1} = \hat{n}_{e_1} \cdot \varphi_{e_1} \tag{19}$$

$$\hat{n}^{A}_{e_1} = \frac{\hat{n}_{e_1} \cdot \varphi_{e_1}}{A_{e_1}} \tag{20}$$

For a node N_i, its normal vector is computed by summation for all the elements containing the node. Denoting by *Nb* the number of neighboring elements containing the same node, the generalized angle-based and area-weighted normals at node N_i can be written as follows:

$$\hat{n}^{\varphi}_{i} = norm\left(\sum_{j=1}^{Nb} \hat{n}^{\varphi}_{e_j} \right) = \left\| \sum_{j=1}^{Nb} \hat{n}_{e_j} \cdot \varphi_{e_j} \right\| \tag{21}$$

$$\hat{n}^{A}_{i} = \sum_{j=1}^{Nb} \hat{n}^{A}_{e_j} = \sum_{j=1}^{Nb} \left(\frac{\hat{n}_{e_j} \cdot \varphi_{e_j}}{A_{e_j}} \right) \tag{22}$$

Pillai *et al.* /17/ proposed an approach to calculate the normal at a node based on the minimization of the net deviation of the projected thickness. A small radius commonly appears in meshes of thin shell parts where the area of the elements strongly varies from the rest of the part. Based on the Pillai *et al.* approach, to account for the influence of the element dimension on the averaged node normal, the extrapolation direction can be computed as follows:

$$\hat{n}_i = \frac{\left(\hat{n}^{\varphi}_i\right)^2 \cdot \hat{n}^{A}_i}{\sum_{j=1}^{Nb} \left((\hat{n}_j \cdot \hat{n}^{\varphi}_i)^2 \cdot \frac{\varphi_j}{A_j} \right)} \tag{23}$$

This solution is appropriate to extrude complex curved surfaces, although it may be limited by the interference between extruded elements. A practical limitation is then imposed between the curvature of the geometry and the thickness to avoid mesh interference during extrusion.

Once the normal at a node has been defined, a group of new nodes must be extrapolated in the normal direction. If the extrapolated node must be extruded by a thickness of *ply_th*, the new node position can be found by a vector summation of the original nodal coordinates $\bar{N}_i$ (coordinates of the node in the 2D mesh) and the normal vector $\hat{n}_i$:

$$\bar{N}^{p}_{i} = \bar{N}_i + \hat{n}_i \cdot ply\_th \tag{24}$$

where $\bar{N}^{p}_{i}$ denotes the extruded nodal coordinates and p is the extrapolation index (or ply number). In general, equation (24) can be transformed to consider the total extrusion thickness *total_th* of the part. For the ply position *ply_ps* defined in percent of total thickness, the new nodal coordinates can be obtained from:

$$\bar{N}^{p}_{i} = \bar{N}_i + \hat{n}_i \cdot total\_th \cdot node\_ps \tag{25}$$

$$node\_ps = (\chi \cdot ply\_ps + \gamma), \quad \text{with } 0 \le ply\_ps \le 1$$

Here, χ and γ are two unitary coefficients. As shown in Figure 6, different extrusion scenarios are possible by combining χ and γ values. These coefficients allow the node extrapolation to be carried out from midplane position in the normal direction (a) or in the opposite normal direction (c). Nodes can also be generated from a position at +/- half thickness (b), or from any position in between. Finally, the use of χ and γ permits the introduction of the ply thickness as a spatial function that varies along the part geometry (d).

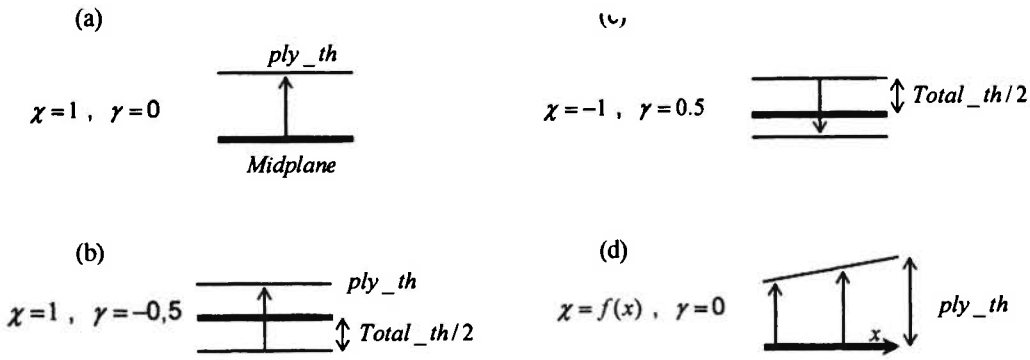

Fig. 6: Selection of the extrusion direction using the χ and γ coefficients of equation (21). (a) the position of the new nodes can be computed from the midplane position; (b) from the half thickness; (c) or in the opposite normal direction; (d) ply thickness can also be set as a spatial function.

After the new nodes have been created, the three-dimensional finite element must be generated following the connectivity of the 2D mesh. Note that material properties and boundary conditions are not necessarily identical for each extrapolated layer, and then cannot be copied from the initial 2D mesh. Next, a data structure will be presented to allow the setup of different materials through the thickness of the part.

Structure of the laminate

A class structure is proposed to define the properties of the layers to be extruded according to the laminate structure. In composite manufacturing, consecutive fabric plies are stacked on the mold surface forming a material lay-up usually called *laminate* or *stacked preform*. As shown in Figure 7, the plies can be of different materials or exhibit different planar orientations, resulting for example in a non-uniform permeability tensor through the thickness. Moreover, ply thickness may vary as they are made out of materials with different compaction behaviours. The laminate data structure must contain, for each ply in the stack, the required information to reconstruct the layer geometry with the associated material properties.

Based on the concept used in PamRTM™ /11/ to

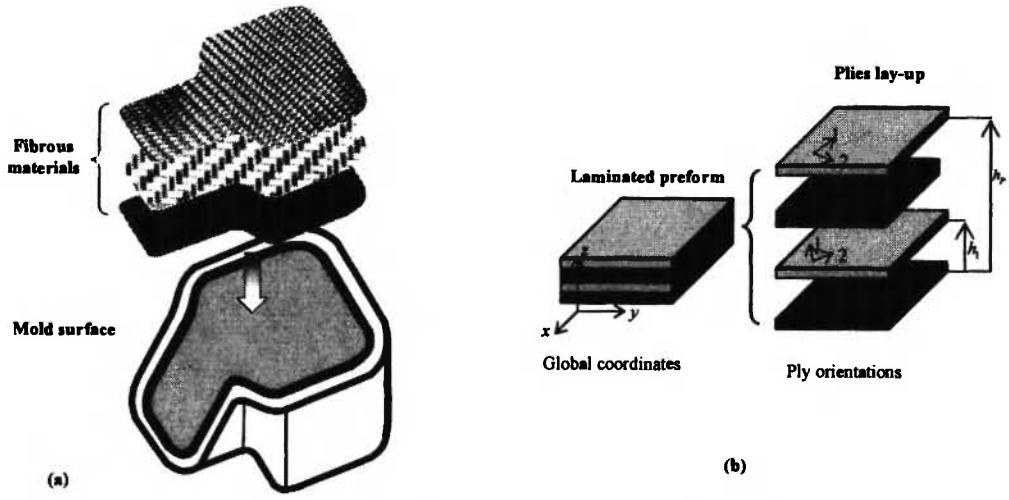

Fig. 7: (a) In composite manufacturing, layers of fibrous materials are stacked to form a compact preform. (b) The plies of the laminate can have different thickness and fiber orientation.

divide the part geometry into zones (see Figure 8), a laminate definition is connected to each mesh zone. The laminate structure contains useful information on ply properties, stacking sequence and direction of extrusion. The subclass *ply* contains a link to the specific fabric material and encapsulates a series of variables including ply thickness, porosity and fabric orientation. If two plies are made out of the same material, but differ in their planar orientation, during extrusion the permeability tensor associated to the two-dimensional finite element is rotated according to the ply orientation. For complex geometries that require draped directions of the fabric preform, a draping analysis may be performed with QuickForm™ /12/ or PamForm™ /13/. Fiber orientations can then be linked to the laminate following the instructions of reference /12/.

This data structure stores the ply information for each zone of the mesh and contains the properties of the finite element for each extruded layer. The division into zones with different laminate structures allows the construction of complex three-dimensional geometries as illustrated in Figure 9. Parts containing out-of-plane ribs can be generated by setting a different number of plies between zones. Thick parts with impermeable foam cores can also be constructed from the 2D mesh and proper laminate definition. In order to demonstrate the capabilities and accuracy of the proposed methodology, laboratory injections inducing through-thickness flow are compared to numerical predictions in two cases: (1) unidirectional flow through multi-layer preform; (2) pointwise injection in a thick composite.

EXPERIMENTAL VALIDATION – CASE I

The experiment performed by Diallo *et al.* /14/ involves the injection of pressurized oil into a rectangular cavity filled with a stack of fibrous reinforcements. Figure 10 shows a schematic of the experimental set-up used to record the flow front position in time. The mold assembly is made of two tempered glass plates of 930 x 130 x 19 *mm*. The mold cavity thickness was set with a 12 *mm* thick spacer. A silicone sealant was used to prevent edge effects along the mold edges. A constant injection flow rate was performed with a hydraulic cylinder mounted on a tensile testing machine. The reinforcement was a thermo-formable glass fabric EB-315-E01-120 from

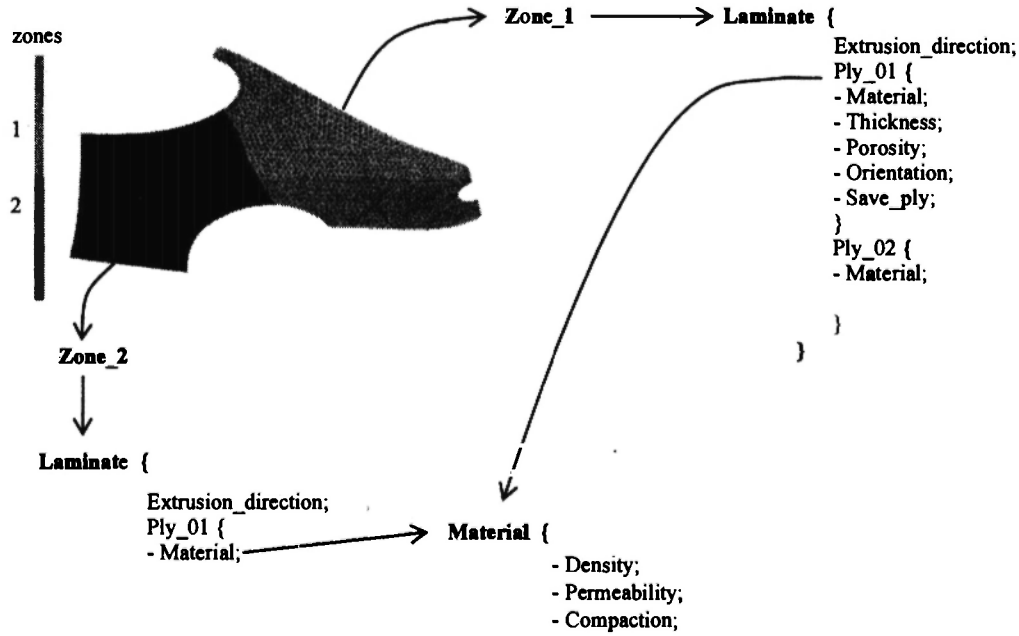

Fig. 8: Data structure used to relate zones of PamRTM /11/ with the structure of the laminate. Each ply of the laminate is related to a fabric material. Multiple zones can be connected to the same laminate and different plies can point to the same material.

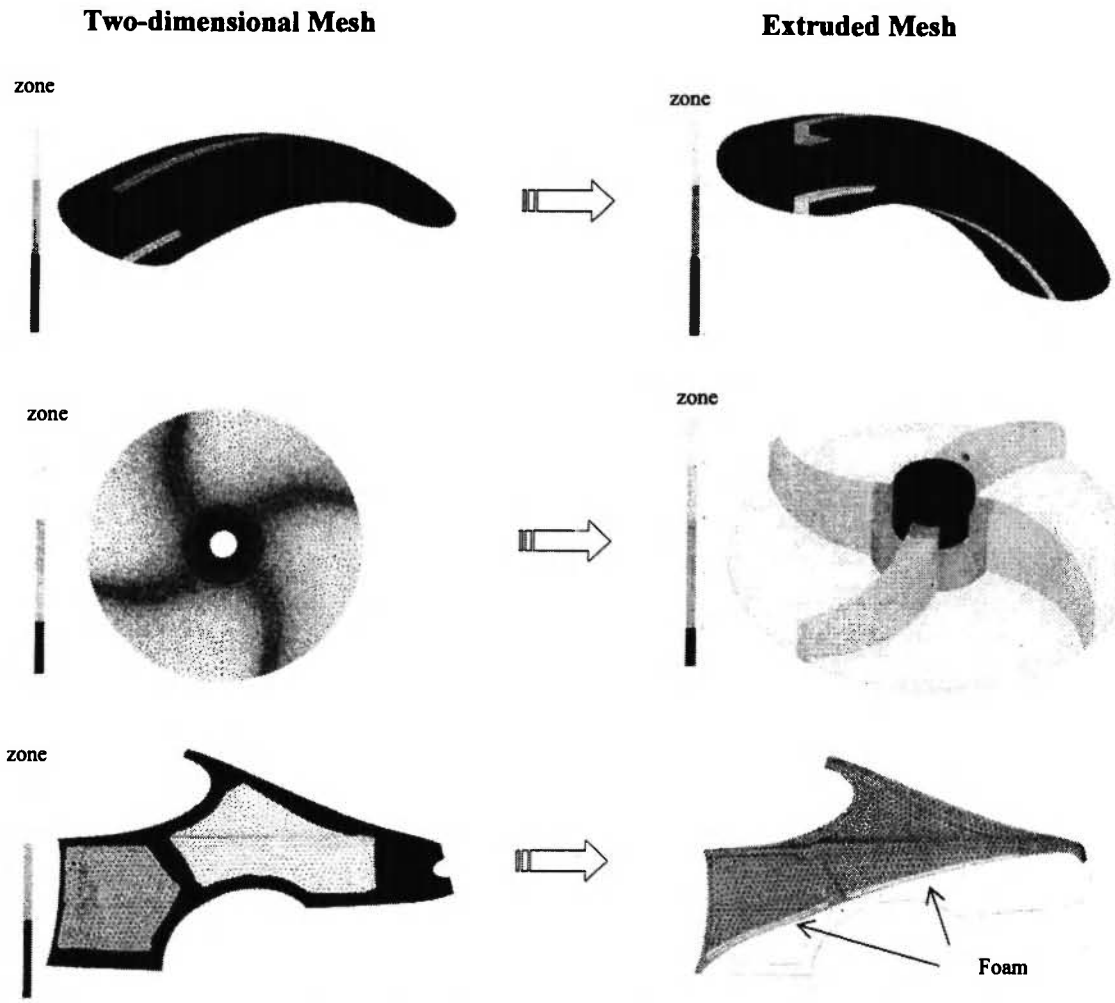

Fig. 9: Typical applications of the extrusion algorithm. Examples of three-dimensional meshes for various stacked materials may be constructed from the midsurface mesh and structure of the laminate.

Brochier, which has an anisotropic permeability and surface density of 315 g/m^2. For this fabric with a fiber volume fraction of 45%, the measured permeability in the weft direction is K_{weft}= $6.5x10^{-10}$ m^2, in the warp direction K_{warp}= $5x10^{-11}$ m^2 and through-thickness K_z= $2.0x10^{-11}$ m^2. The oil viscosity measured at room temperature was 0.103 *Pa.s*. As illustrated in Figure 10, 20 small wires of 0.1005 circular inches (~0.35 *mm* diameter) were inserted between the reinforcement plies to measure the shape of the through-thickness flow front. One wire was placed at the injection port and used as ground. As the oil impregnates the wires, an electrical contact is established and the position of the flow front can be recorded in time.

In order to create a through-thickness flow, the preform was constructed from the superposition of 20 plies of fabric materials aligned in the weft direction, and 20 plies aligned in the warp direction. The upper plies form a high permeability layer that speeds up the flow, while the low permeability of the lower plies delays the flow. In this experiment, the injection flow rate was maintained constant at 3.04 *cc/s*. To simulate this laboratory injection, the three-dimensional mesh of Figure 11 was generated using prismatic (6 nodes) finite elements. As shown in Figure 11, the 3D model is a brick of size 500 *mm* x 12 *mm* x 20 *mm* with 4 *prism6* elements per layer (a total of 8 finite elements through the thickness). The injection boundary condition is set

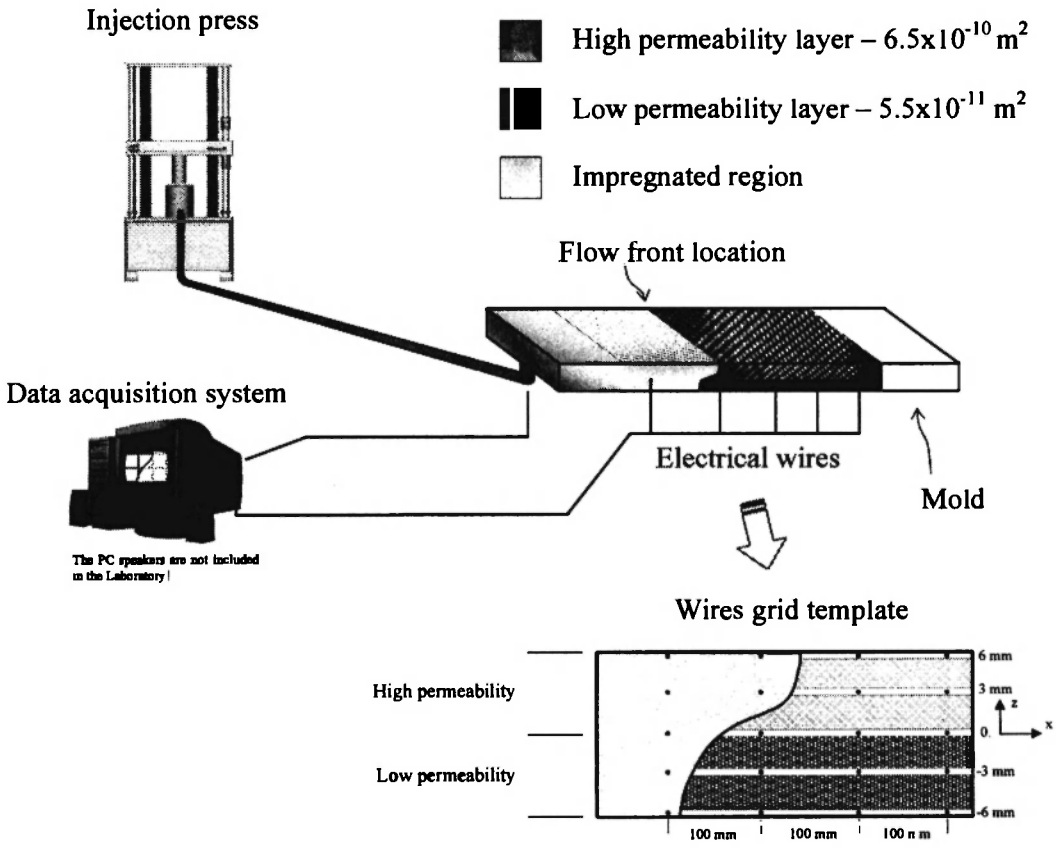

Fig. 10: Schematic diagram of the through-thickness flow front shape measurement system used by Diallo *et al.* /14/.

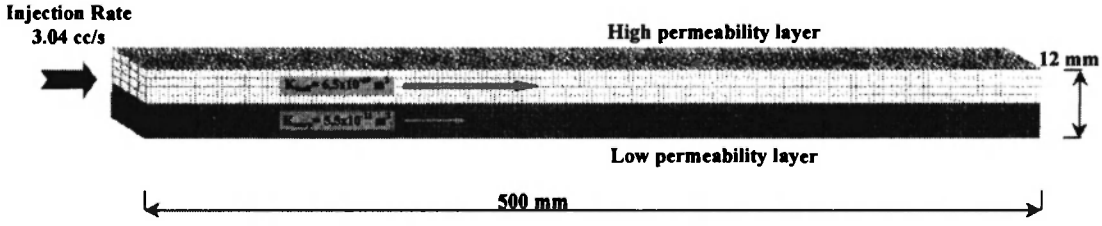

Fig. 11: Three-dimensional model used to simulate the experiments of Diallo *et al.* /14/. In each layer of the laminate the mesh contains 4 *prism6* finite elements in the through-thickness direction.

on the faces of the finite elements on the left side of the plate.

A comparison of the experimental flow with the results of the simulation can be seen in Figure 12. At the start of filling, a distortion in the flow front develops quickly (for injection times less that 20 *sec.*). Afterwards the two in-plane flows reach an equilibrium state and the distortion is stabilized. The progression of the flow front on the bottom and top mold surfaces is in good agreement with experimental results. The caption of Figure 12 shows the through-thickness profile of the flow at 88 seconds, which corresponds very well to the measures of the electrical wires.

Since the *prism6* element does not ensure continuity

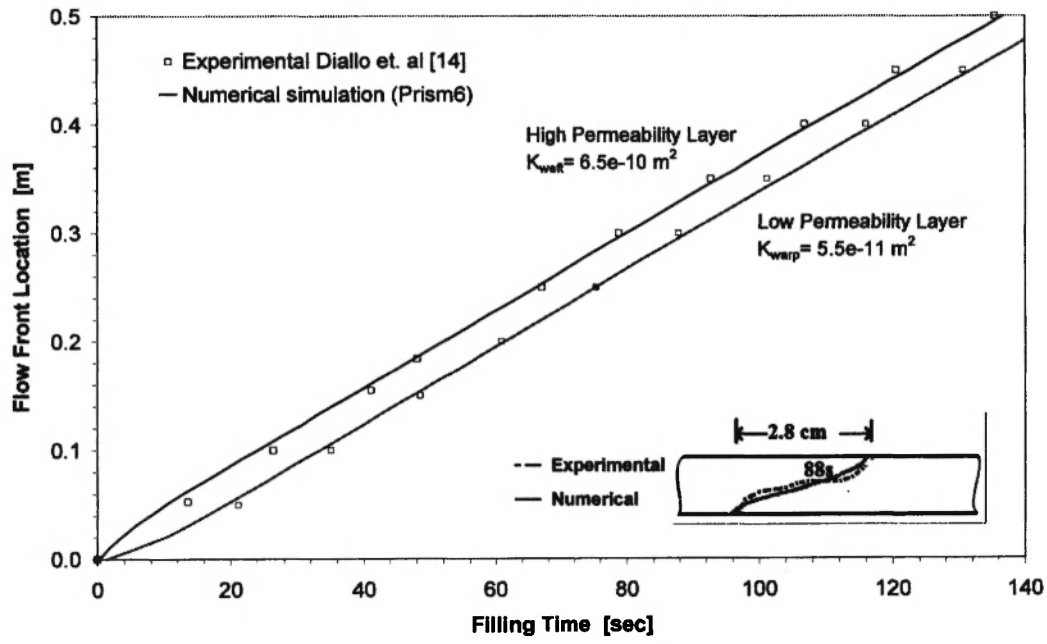

Fig. 12: Flow front progression in the top and bottom mold surfaces. The flow front distortion is stabilized after 20 sec. The numerical through-thickness front at 88 seconds is shown in the bottom right caption and is very close to the experimental profile.

of the resin mass following through the thickness of the composite as it does for the in-plane flow, the fluid mass lost may affect the flow front geometry. To quantify the error in the solution arising from this, a series of five simulations were carried out. As listed in Table 1, the permeability ratio between the upper and lower layers changes from 1 (no transverse flow) to 6 (high transverse flow). The approximate solution obtained with the new finite element is compared with the experimentally validated two-dimensional solution of PAM-RTM calculated with triangular non-conforming finite elements. A simulation with non-conforming tetrahedral elements is taken as reference of the performance of the three-dimensional solution. The triangular mesh contains 5,700 elements divided into 16 layers through the thickness (see Table 2). The *prism6* mesh was decomposed into 17,000 elements and 16 layers, while the tetrahedron mesh has 65,500 elements and 24 layers (required to conserve the aspect ratio of the tetrahedrons). Note that tetrahedrons must not be degenerated to ensure convergence of the solution. This implies an aspect ratio close to one, i.e. height and planar dimensions are of the same order of magnitude.

Table 1

Series of test carried out to quantify the resin mass loss when using *prism6* finite elements.

Permeability (x10 ^{9} m^2)			
Test #	**K_1**	**$K_2 = K_Z$**	**K_1/K_Z**
1	2	2	1
2	1.5	1	1.5
3	1	0.5	2
4	0.75	0.1875	4
5	0.5	0.0833	6

Table 2

Description of the 2D and 3D meshes used to compare the error on the mass loss.

Geometry of the FE's	Number of Finite Elements		
	Thickness	**Length**	**Total**
Triangles	16	710	5700
Prism6	16	330	17000
Tetrahedrons	24	270	65500
Part dimensions : 500x12x12 mm			

If the thickness of the part is small compared to its area, the number of tetrahedrons required for a proper solution is extremely high. The numerical simulations were carried out on an IBM IntelliStation M-Pro PC with a Pentium III (1.0 GHz) processor.

For the five cases tested, the progression of the flow front at the interface between the two zones of different permeability (at half thickness) is displayed in Figure 13 for different anisotropy ratios. The flow front progression in the mid-plane is representative of the averaged flow and is expected to fit between meshes if no mass is lost during filling. The calculation for the highest anisotropy ratio required less than 25 minutes to run with the triangular mesh of 5,700 elements. The same case took around 36 hours to compute with the 65,500 tetrahedrons of the 3D mesh, while the *prism6* model needed nearly 5 hours. The strong cpu time reduction is due to differences in the number of degree of freedoms of the models. A comparison of mass lost at the end of filling is shown on Figure 14. The mass loss is calculated as the difference between the injected flow rate along the inlet channel and the flow rate at the flow front location. After filling, the total injected mass must equal the free volume in the mold cavity. The error on the mass loss remains in all cases smaller than 3%. It is maximum for tetrahedrons, and minimum for triangles. The cause of the mass loss with the non-conforming tetrahedrons is connected with the aspect ratio which was no longer equal to 1, but decreased to around 0.6. Note that the mass loss in the *prism6* solution is of the same order of magnitude as that of the triangular mesh.

The *prism6* elements are expected to conserve the fluid mass across their rectangular faces, but not across the thickness (triangular faces). Since the thickness is small compared to the longitudinal extension of the part, the mass lost through the thickness is a small quantity of the total injected mass. This means that even if the total mass seems to be conserved, the flow front geometry may disagree with the 2D solution (triangular mesh). To quantify this error, an estimator was used based on the difference in the through-thickness flow profile between the prismatic or tetrahedron meshes and the triangular model (see Figure 15). The values presented in that figure are the sum of the two differences in the positions of the flow front at the upper and lower mold surfaces. It is remarkable to note that the mass loss induces a distortion of the flow profile. The *prism6* elements give a less accurate solution than tetrahedrons. Although the

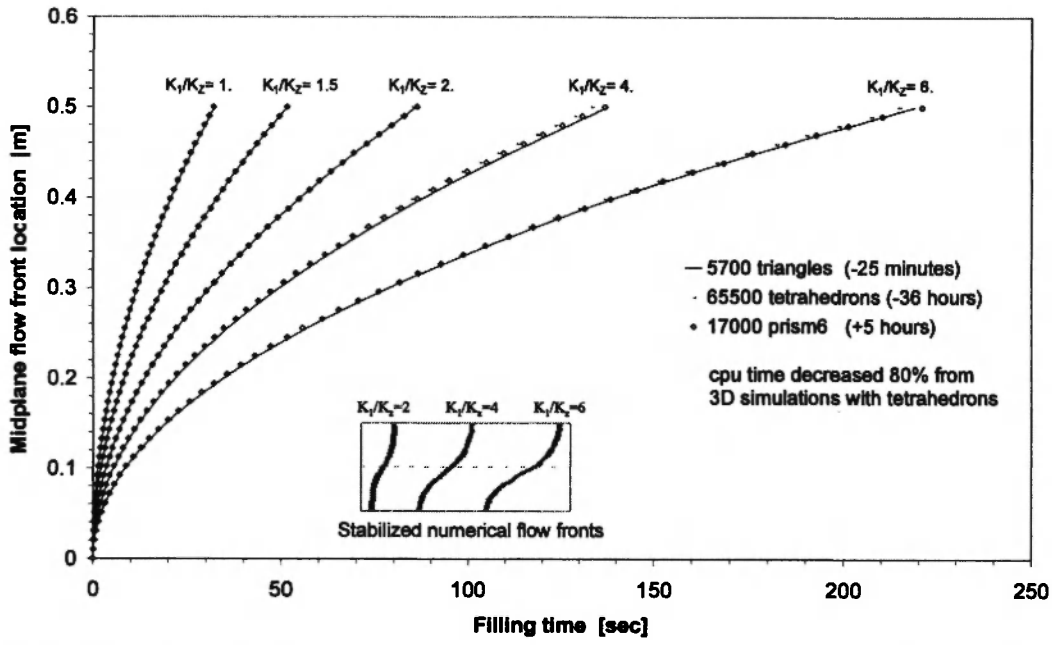

Fig. 13: Progression of the flow front in the midplane for different anisotropy ratios. Compared to the two-dimensional (triangles) solution, the tetrahedron and prism6 solutions predict well the filling at the interface.

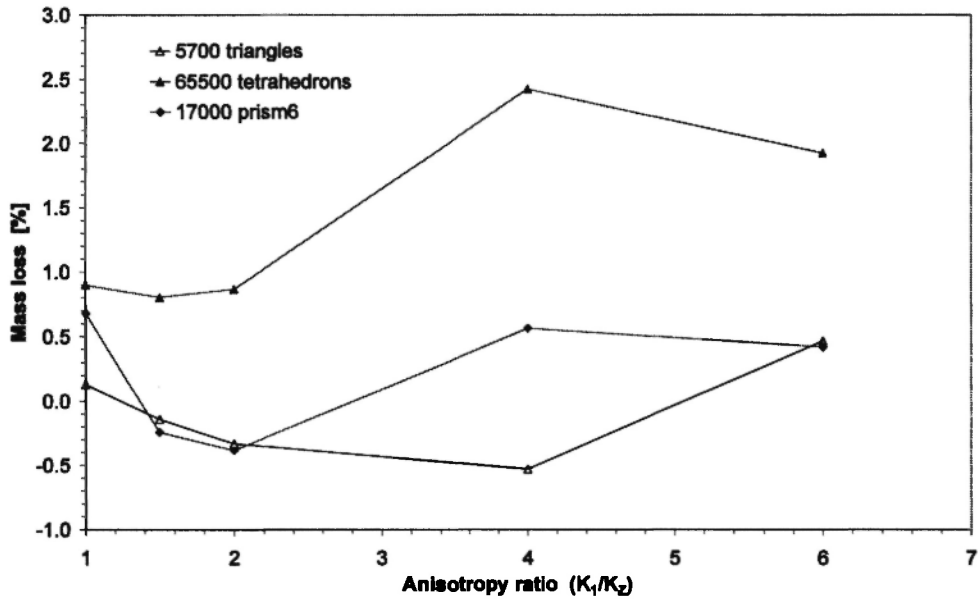

Fig. 14: Comparison of mass loss for simulations with triangles, tetrahedrons and *prism6* elements. In all cases, the mass loss is less than 3%. The *prism6* solution is systematically more conservative than tetrahedrons and close to the triangle solution.

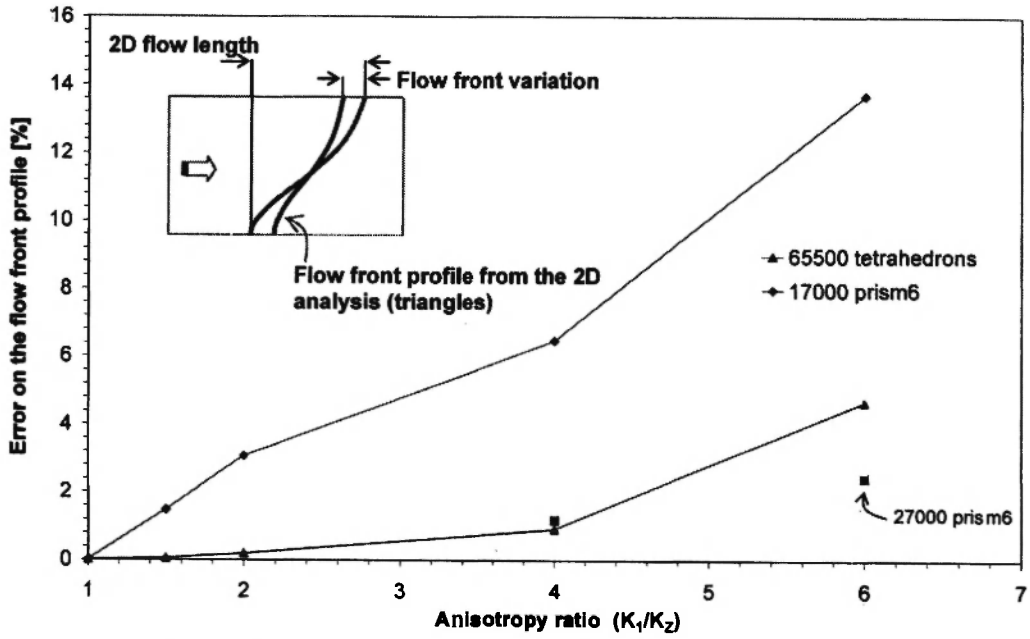

Fig. 15: The distortion of the through-thickness flow front profile for *prism6* and tetrahedrons is compared to a 2D reference simulation (triangles).

error seems more important for the prismatic elements, note that the number of degrees of freedom in the tetrahedron mesh is much larger than in the *prism6* model. When the number of though-thickness layers in the *prism6* mesh was increased to 24 (i.e. a total of 27,000 *prism6* elements), the flow front error was reduced to similar values as that of the tetrahedron solution and even to a lower value for higher anisotropy ratios.

EXPERIMENTAL VALIDATION – CASE II

As a further validation exercise, the proposed numerical method was compared with experiments in the case of a spherical 3-dimensional flow. Bréard /15/, has performed central injections in a thick mold containing an anisotropic reinforcing material. This result was used in Breard and Trochu /18/ in a comparison with the numerical solution of LCMFlot software. The position of the spherical 3D flow front was detected by X-Ray radioscopy. As drawn in Figure 16, in this example the rectangular mold is an internal cavity volume of 300 x 300 x 20 mm^3. Silicon oil was injected through the cylindrical inlet (*5 mm* diameter) from the centre of the mold. The injection pressure was 1.89×10^5 *Pa*, and the silicon oil viscosity 0.1 *Pa.s*. The in-plane permeability of the porous material used was $K_X = K_Y = 3.95 \times 10^{-10}$ m^2, and the transverse permeability $K_Z = 9.3 \times 10^{-11}$ m^2. The anisotropy ratio between the in-plane and transverse permeabilities is $K_X/K_Z = 4.25$.

A three-dimensional mesh was constructed to discretize a quarter of the rectangular mold with *Prism6* elements extruded in the thickness direction. The model contains around 30 elements along x and y axes, and 50 elements in the transverse direction (z axis). Elements are refined around the injection gate to ensure a good reproduction of the boundary condition. Figure 17 shows a comparison of predicted and measured flow fronts in the spherical injection. Simulated flow fronts correlates very well with experimental observations, although a small divergence is observed at the beginning of the injection (prior to 2 *sec*). The reason of these differences between experimental flow front locations and numerical calculations may be explained by the preform compaction surroundings the injection gate at the beginning of the injection.

To quantify the error on the flow front prediction, a comparison with an elliptic three-dimensional flow was carried out. Consider a cavity similar to the previous experimental case, but filled with an isotropic material. The flow front position at time t_{fill} can be obtained by

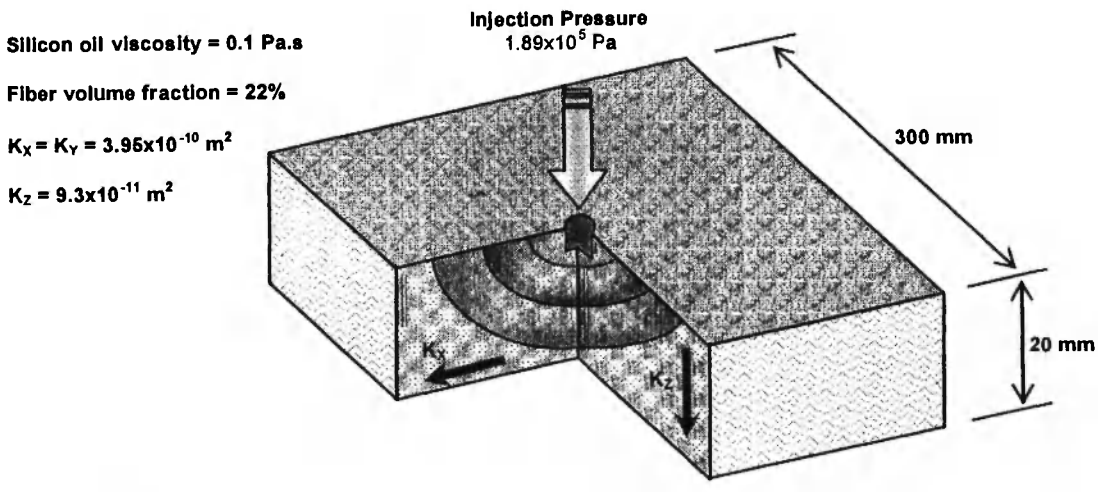

Fig. 16: Schematic drawing of a spherical central injection. The fibrous preform has an anisotropy ratio of 4.25 between the planar and transverse permeabilities. X-Ray radioscopy was implemented to detect the progression of the three-dimensional fluid flow (Bréard *et al.* /15/).

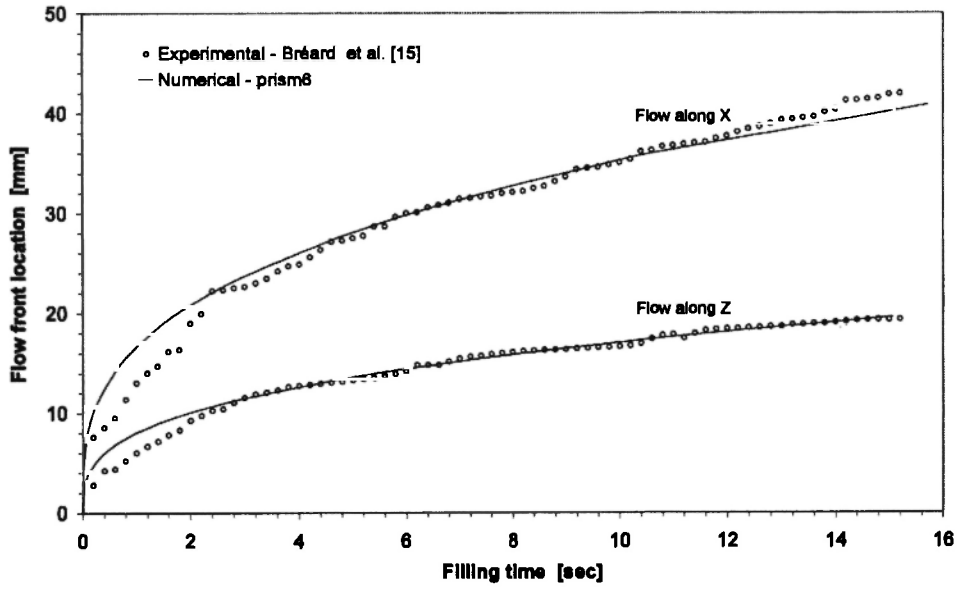

Fig. 17: Comparison of predicted and measured flow fronts in the spherical injection. Numerical results are in good agreement with experimental values.

solving Darcy's equation for an elliptic flow:

$$t_{fill} = \frac{\phi\mu}{6K}\left(R_f^2\left(2\left(\frac{R_f}{R_0}\right) - 3\right) + R_0^2\right)\frac{1}{\left(p_0 - p_f\right)} \qquad (26)$$

where K is the isotropic permeability and R_0, R_f denote respectively the injection gate radius and the position of the flow front. The properties considered here are a permeability K= 1e-10 m^2, a porosity of 0.5, a fluid viscosity of 0.1 *Pa.s* and an injection radius of 1.12 *mm*, while the relative injection pressure p_0-p_f was set to 1e5 *Pa*. Meshes were constructed with different numbers of elements in the radius direction. *Prism6* and tetrahedron elements were used to run a series of filling simulations. Figure 18 shows a comparison of the numerical results with the three different meshes. Note that the mesh with 30 *prism6* elements in the radius direction shows a better agreement with theoretical values than the mesh with 50 tetrahedrons. The error on the flow front prediction at the end of filling can be seen in Figure 19. The convergence of the *prism6* mesh is higher than for tetrahedron elements. For the same number of elements along the radius, the *prism6* mesh gives a smaller error on the flow front estimation than tetrahedrons. Remark that, in this analysis, the fluid flow occurs in a three-dimensional space. The pressure gradient in the x, y and z directions will be of the same order of magnitude. Although this comparison is very convincing about the ability of the proposed model to predict three-dimensional flows, a loss of fluid mass appears due to the *div-non conformity* in the through-thickness direction. Therefore, even if the flow front is well predicted, some fluid mass may be lost during the filling simulation due to the accuracy of the through-thickness solution of *prism6* elements.

CASE STUDY – TRUCK FENDER

In order to demonstrate the practical validity of the proposed solution, the three-dimensional mesh extrusion and mold filling analysis are carried now for a typical LCM automotive part. The objective of this test is to demonstrate the advantage in terms of user time of a quick methodology to simulate irregular flows in a

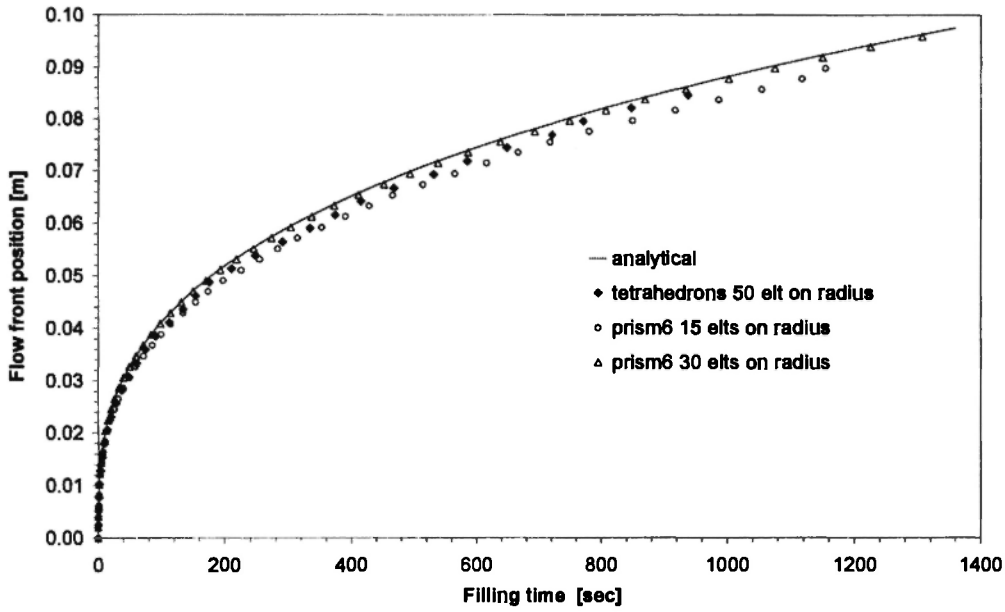

Fig. 18: Comparison of flow front positions calculated for different mesh sizes with the theoretical solution of an elliptic flow through an isotropic material.

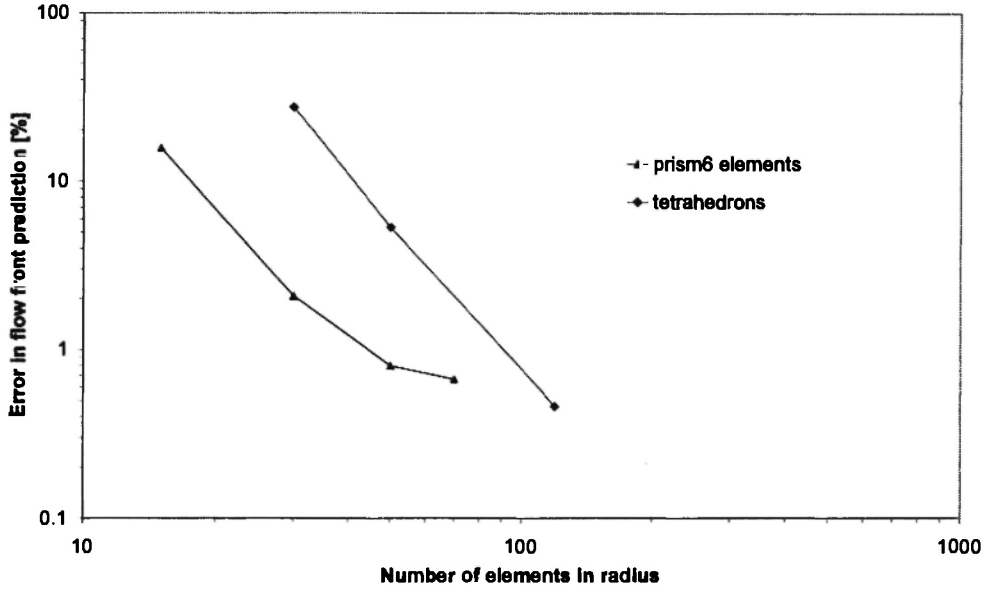

Fig. 19: Convergence of mesh refinement for the elliptic flow through an isotropic material. For the same number of elements on radius, the *prism6* solution yields better results than the tetrahedron one.

complex geometry. The truck fender of Figure 20 has a complex three-dimensional shape of variable thickness, and contains different fibrous materials and stacking sequences. The finite element mesh generated from the CAD geometric model 17,000 triangular elements and 8,500 nodes. The part is decomposed into 13 zones with different laminate structures.

In LCM, because of the cutting of the fibers and the free space created along the mold edges, the fluid (resin) may flow through a preferential path along the edges of the part. This phenomenon, called *edge effect* or *race tracking*, can be numerically modeled using an enhanced permeability in the elements located along the edges /16/. During mold closure, preform interference often appears in surfaces with double curvature, in straight chamfers or in fillets with different internal and external radius. These draping problems create fiber or void rich zones that strongly influence the flow during mold filling. In some cases, the fluid flow is faster in these regions (resin rich zone) than in the adjacent preform. In other cases, the flow slows down in regions of high fiber volume content and surrounds the low permeability zones. In the fender model, diverse draping problems are considered, which translate into zones of higher or lower permeability and porosity.

The injection strategy consists of four inlet gates and two vents placed all around the part. The two inlet gates at the upper corners (1 and 2 in Figures 20 and 21) are connected to an open channel free of any reinforcement. This channel allows a quick evolution along the part length (x-axis) and then distributes the resin vertically. This filling strategy is usually called a peripheral injection. Inlet 3 is also connected to an open channel at the end of the stiffener. This strategy is used to ensure a proper impregnation of the longitudinal rib. Injection gate 4 is positioned at the interior of the light support, where the laminate is made out of different materials. This central injection gate permits to fill up the low permeability zone containing the above mentioned laminate. For all injection gates, the injection pressure is maintained constant at 3.0×10^5 *Pa*. An isothermal resin viscosity of 0.1 *Pa.s* was used for this analysis. To expel the air from the mold, two vent points are set: one at the center of the elliptic shape (vent 1), and the other one in the fender lower corner (vent 2). The vent in the elliptic shape of the part is closed when the resin arrives to it.

The laminates associated to each zone of the part are defined in Table 3. A maximum of six layers were used in the stiffener and in the light support. In zone 10, an impermeable foam core is wrapped by two fabric skins. The layer on the surface of the part has a lower permeability than the hidden ply; this can be explained by a non-uniform compaction of the double curvature foam core. Race tracking effects are modeled around the foam core (zone 7) to reproduce the resin rich zone along the foam edges. At the intersection between planar surfaces where straight angled chamfers appear, a lower permeability is considered locally (zones 2, 3, 6 and 8). Figure 22 shows the final three-dimensional model after the triangular mesh extrapolation is carried out based on the laminate structure. The open channels in the upper edge of the part, as well as the foam core, are meshed in detail. The whole model contains 60,000 prismatic elements and 40,000 nodes.

The performance of the proposed methodology and numerical extrapolation scheme is compared with the solution of the shell model. To compute both cases, the same mesh and laminate definition are entered in the input data of the program. If no extrapolation is required, the program automatically computes the gapwise average permeability of the laminate according to the classical weighted average:

$$\bar{K} = \frac{\sum_{i=0}^{Nl} h_i \cdot K_i}{\sum_{i=0}^{Nl} h_i} \tag{27}$$

with

Nl : number plies in the laminate
h_i : thickness of the i-ply.
K_i : permeability of the i-ply.

Predicted filling times for the shell model with averaged permeabilities are given in Figure 23. This calculation required 44.5 minutes to run on a IBM IntelliStation M-Pro PC with a Pentium III (1.0 GHz) processor. An injection time of 24.5 *sec* was obtained when the resin arrived to the second vent. The flow front profiles clearly show that resin runs along the upper open

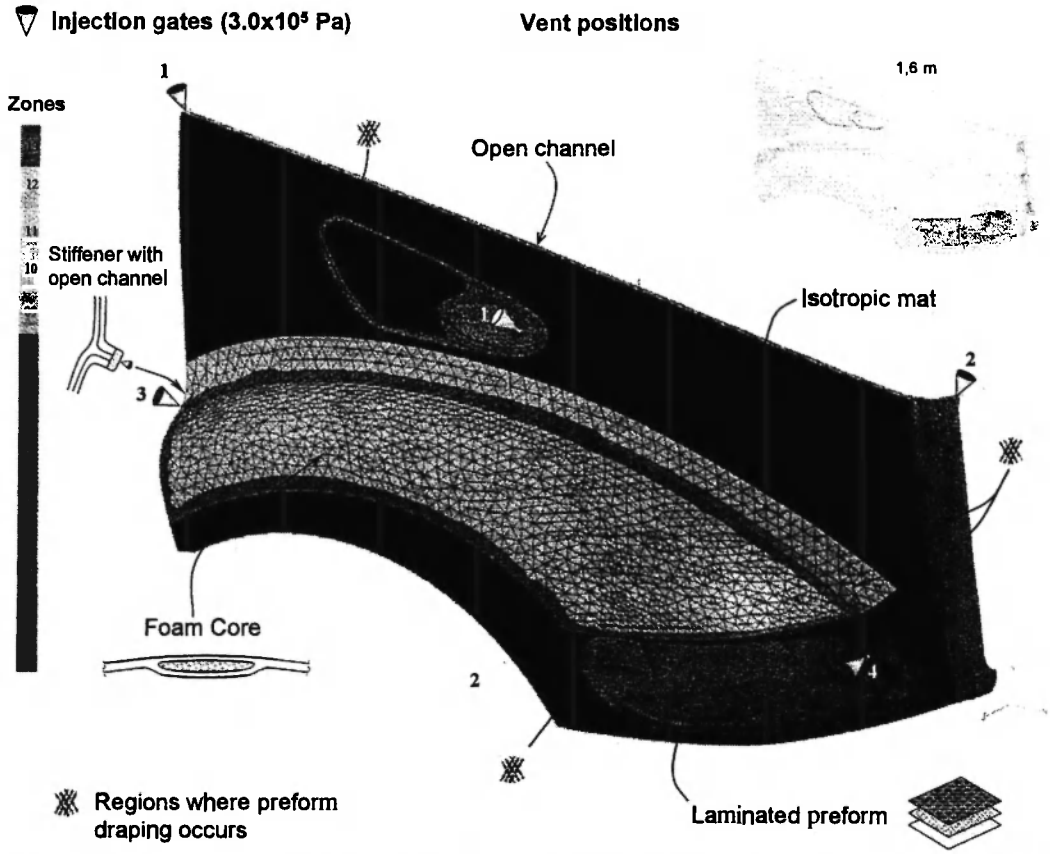

Fig. 20: a Typical LCM part used to demonstrate the capabilities of the model. The mesh contains 17,000 triangles and 8,500 nodes. The injection strategy consists of four inlet gates at the upper part corners, at the stiffener ends, and in the laminated zone. An impermeable foam core is wrapped by fabric skins in zone 10. Draping effects are represented as regions with high or low permeabilities.

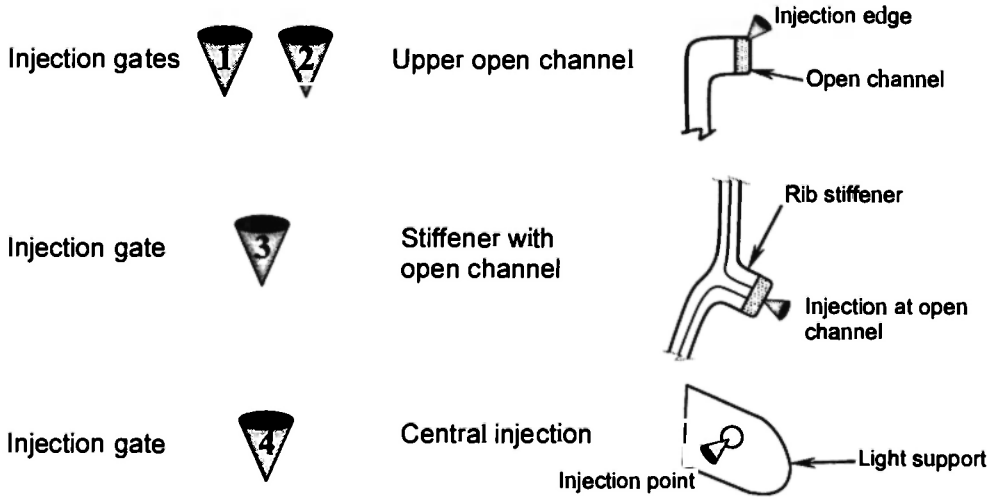

Fig. 21: Injection strategy used for the truck fender. Four injection gates are set in the mold. Open channels are used for a better distribution of the resin flow. To ensure filling of the stiffener, an open channel is created at the extremity of the rib.

Table 3

Permeability and porosity for each zone of the truck fender model.

Zone Id	Ply # ⟶	1	2	3	4	5	6
1	porosity	0.8					
	thickness [mm]	5					
	permeability 10^{9} [m^2]	2					
2	porosity	0.8	0.8	0.8	0.8		
	thickness [mm]	5	5	5	3		
	permeability 10^{9} [m^2]	0.3	0.3	0.3	0.3		
3	porosity	0.6					
	thickness [mm]	5					
	permeability 10^{9} [m^2]	0.3					
4	porosity	0.8	0.8	0.8	0.8	0.8	0.8
	thickness [mm]	5	3	3	5	2	2
	permeability 10^{9} [m^2]	3.5	3.5	3.5	0.7	0.7	0.7
5	porosity	0.8					
	thickness [mm]	5					
	permeability 10^{9} [m^2]	0.8					
6	porosity	0.6					
	thickness [mm]	5					
	permeability 10^{9} [m^2]	0.3					
7	porosity	0.8	0.8	0.8			
	thickness [mm]	5	6	6			
	permeability 10^{9} [m^2]	3.5	3.5	3.5			
8	porosity	0.6					
	thickness [mm]	5					
	permeability 10^{9} [m^2]	0.3					
9	porosity	0.8					
	thickness [mm]	5					
	permeability 10^{-9} [m^2]	2					
10	porosity	0.8	0.8	0.8			
	thickness [mm]	5	10	7			
	permeability 10^{9} [m^2]	0.8	Foam	2			
11	porosity	0.75	0.75				
	thickness [mm]	3	3				
	permeability 10^{9} [m^2]	1.5	1.5				
12	porosity	0.99	0.99	0.99			
	thickness [mm]	4	3	3			
	permeability 10^{-9} [m^2]	100	100	100			
13	porosity	0.8	0.8	0.8	0.8	0.8	8
	thickness [mm]	5	6	6	3	3	3
	permeability 10^{9} [m^2]	1.5	1.5	1.5	1.5	100	100

channel (between gates 1 and 2) and through the vertical right panel (below gate 2). Resin also flows horizontally in the stiffener zone from gates 3 and 4. Possible dry spots have been detected at the interference between the upper descending and the central ascending flows (denoted as "*D*" in Figure 23). The calculated flow front distribution in the light support is uniform and does not show any impregnation problem. About 8 seconds after the beginning of injection, the resin fronts merge and enclose an air bubble trapped in the center of the part. The air in the bubble exits through the vent gate 1. Approximately at 20 seconds, the resin arrives to vent 1, which is automatically closed. This generates a dry spot. At the end of filling (after 21 *sec.*), the resin flow in the

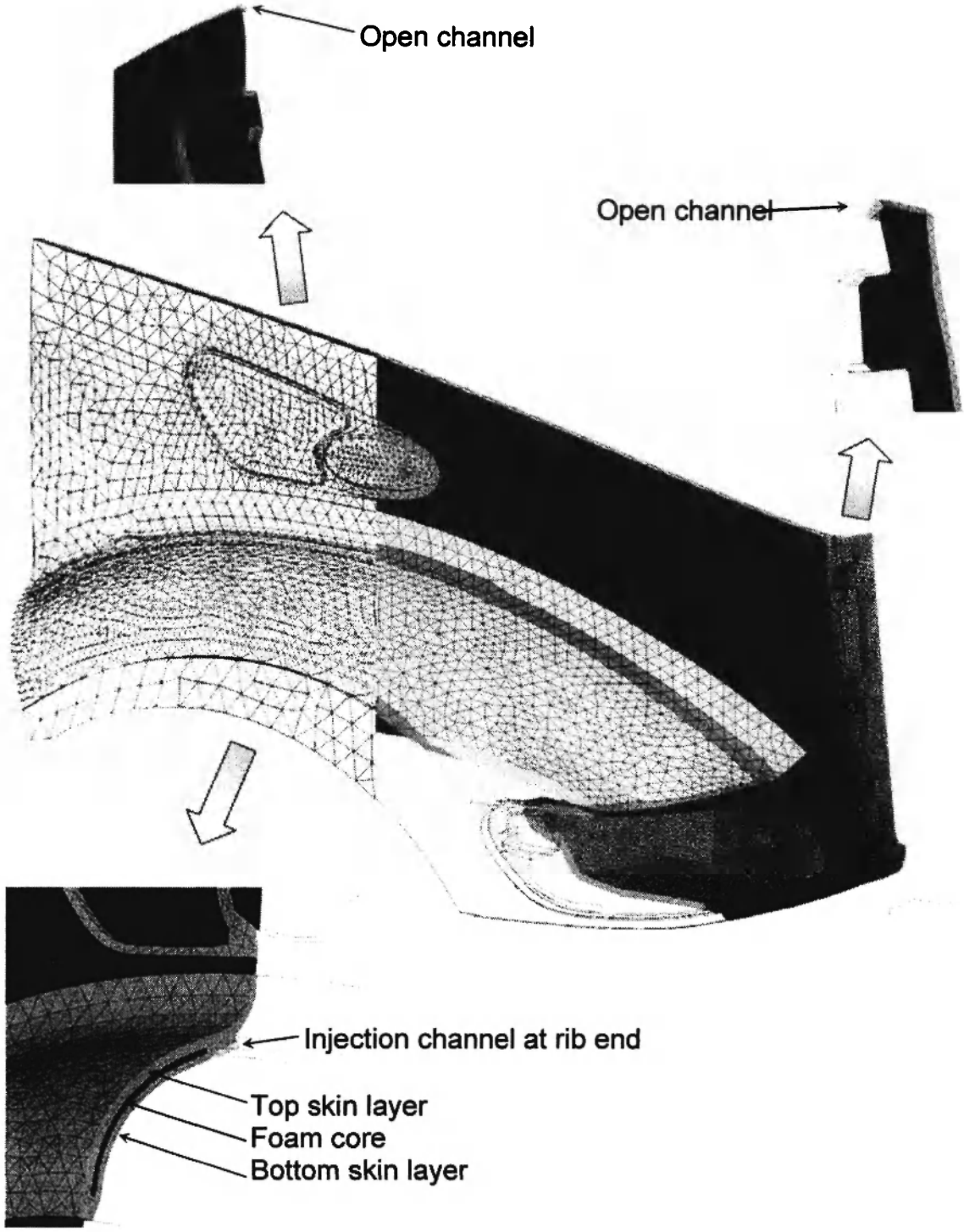

Fig. 22: Three-dimensional model obtained after mesh extrusion. The mesh contains 60,000 *prism6* elements and 40,000 nodes.

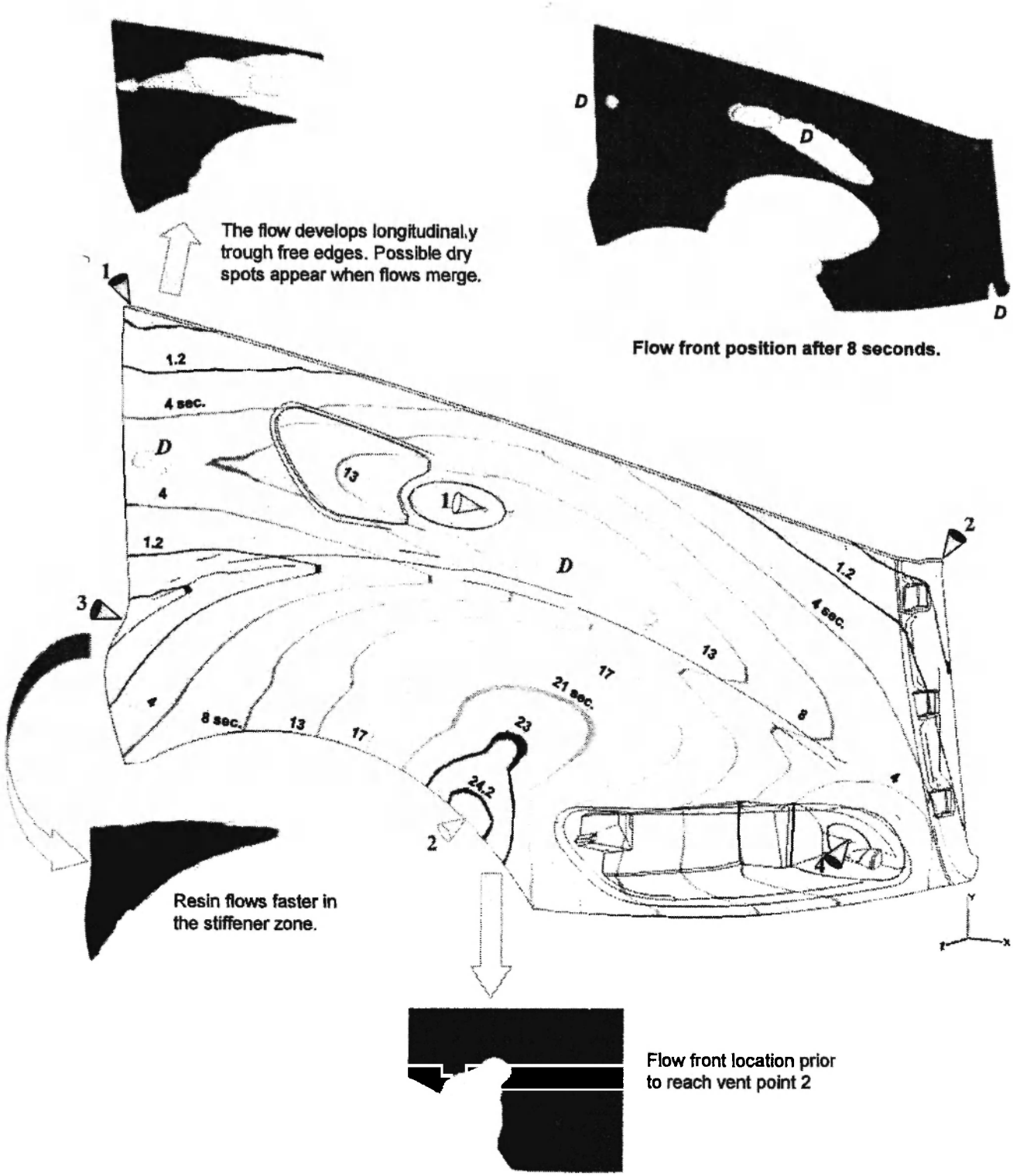

Fig. 23: Predicted filling times with the triangular mesh for through-thickness averaged permeabilities. A total filling time of 24.6 *sec* was calculated. "*D*" indicates possible dry spots.

foam takes the shape of a bubble, although no dry spots were numerically detected.

For the extrapolated three-dimensional mesh, the resulting flow front progression is shown in Figure 24. This solution took 9.5 hours to run on the same computer. A total filling time of 30.6 *sec* was obtained with this model (25% more than previous solution). Although the shapes of the flow front profiles are in general similar in all the simulations carried out, important differences can be noted. In the 2D model, the resin runs faster in the open channels principally along the rib stiffener. In the 3D solution, the modeling of the rib with an open channel results in a transverse flow that differs from the 2D prediction (see details in Figure 24).

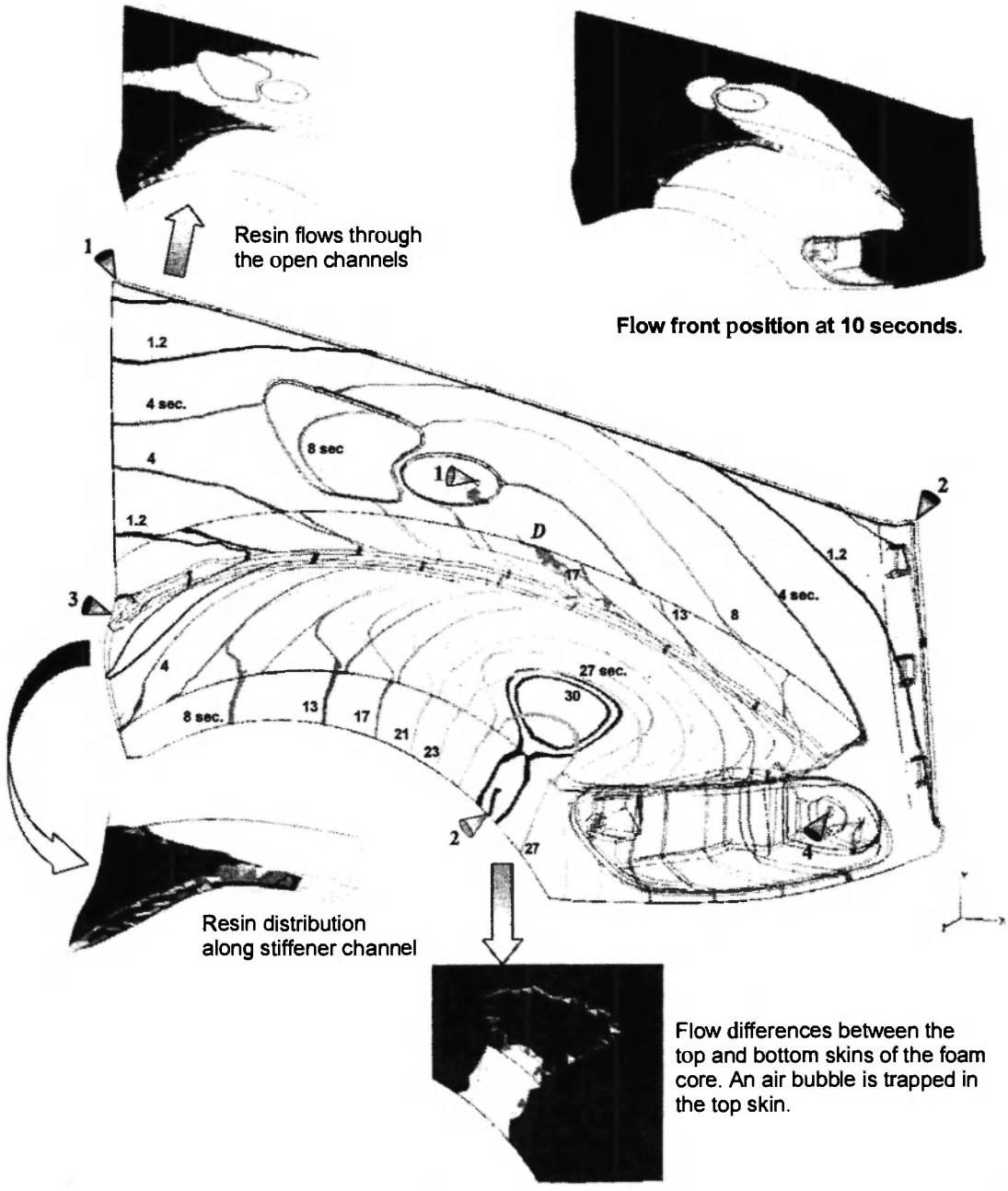

Fig. 24: Predicted flow front locations with the prismatic mesh with multi-layer extrapolation. A total filling time of 30.6 *sec* was calculated. An air bubble was trapped in the upper foam skin.

As a consequence of this three-dimensional flow, the dry spots in the part center were not detected in the 3D model. At around 17 *sec.*, the upper descending and the central ascending flows meet without air trapped between them. In the zone with a foam core, the flow predictions vary for the top and bottom skins, while the 2D model gives the average flow location. This difference in the flow between layers creates an air bubble in the top foam skin close to vent 2. This entrapped air is not detected in the 2D solution, even if the permeability of the foam zone is changed. The results of the 2D model with different permeabilities are illustrated in Figures 25 and 26. The zone with a foam core was assumed to have the permeability of the top or bottom skins, respectively. In none of the two cases, the entrapped air bubble could be detected numerically.

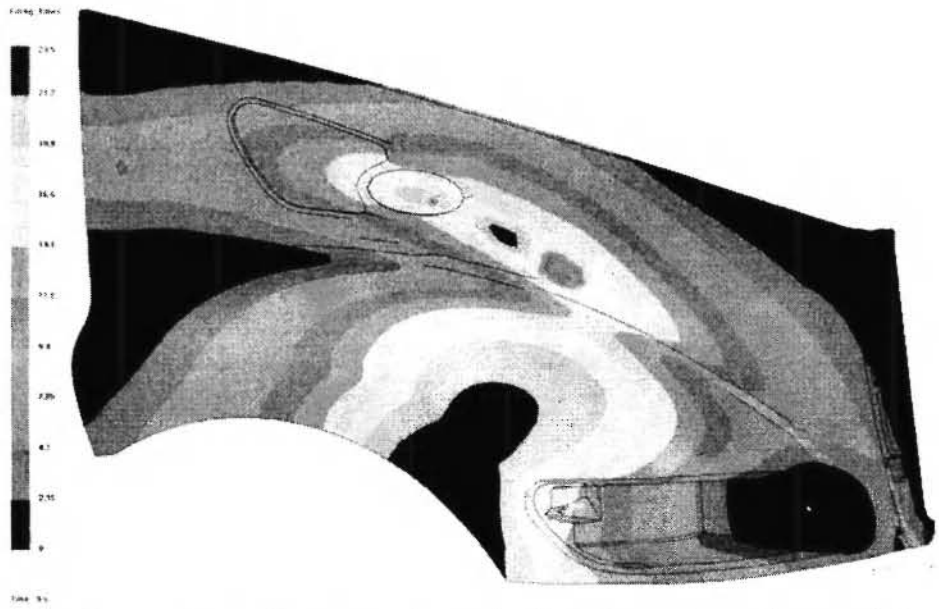

Fig. 25: Predicted flow front positions with the triangular mesh with the *bottom* foam skin permeability. A filling time of 23.5 *sec* was obtained.

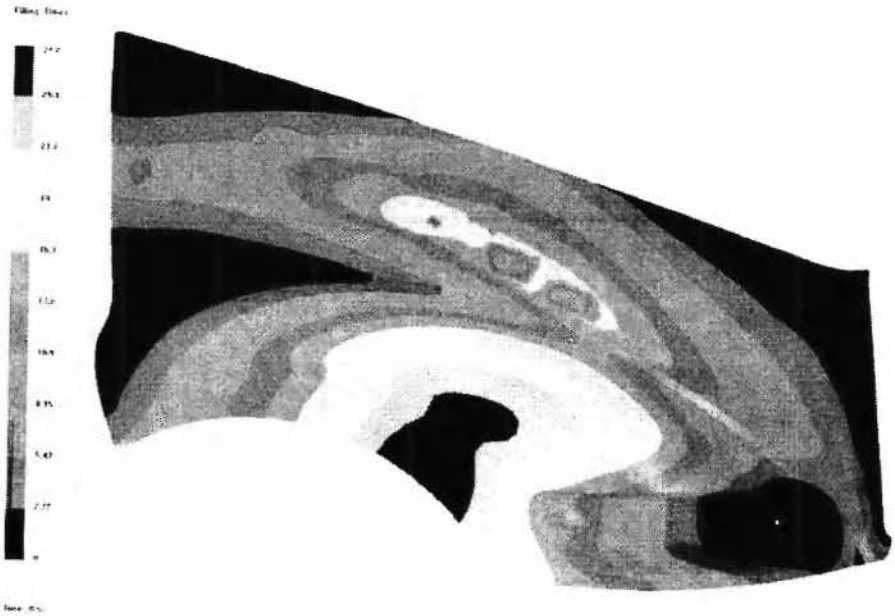

Fig. 26: Predicted flow front positions with the triangular mesh with the *top* foam skin permeability. A filling time of 27.2 *sec* was calculated.

SUMMARY

In this paper, a new methodology is proposed to compute three-dimensional flows in LCM. The method is based on a new *non-conforming* finite element approximation and on a mesh extrusion algorithm to generate three-dimensional multi-layer finite element mesh well suited for composite analysis. Beginning with a thin shell mesh, a solid mesh is constructed by extrusion from the 2D finite element shell mesh. The extrusion is defined by the preform stacking sequence of the reinforcement. This makes it possible to consider different fabric permeabilities and fiber volume fractions in each laminate ply. Boundary conditions may also be extruded through the thickness or set on the top or bottom part surfaces. The development of a new prismatic non-conforming finite element approximation provides accurate through-thickness solutions that minimize the number of elements. This methodology presents several advantages in addition to being user friendly and to facilitate the mesh generation for LCM application. Numerical extrusion gives also the possibility of saving computer time before and after processing. It also minimizes considerably the number of 3D finite elements required to calculate accurate solutions of the flow problem, and hence reduces the computer time as well.

The proposed method has demonstrated a good performance to calculate with good accuracy complex three-dimensional flows without having to create a 3D mesh. Although the required computer time is higher than for the 2D solution, the methodology remains simple thanks to the automatic generation of the 3D mesh by extrusion. The quality of the numerical results is equivalent to that of a full 3D solution with tetrahedrons, but with a great reduction in computer time.

ACKNOWLEDGEMENTS

The authors thank the *National Science and Engineering Research Council of Canada* (NSERC) and *Fonds Quebecois pour la Recherche sur la Nature et la Technologie* (FQRNT) for their financial support. The contribution of *ESI_Group* and their numerical support is also gratefully acknowledged, as well as the program of *Bourses d'Excellence du Ministère de l'Education du Quebec* that made this research possible.

REFERENCES

1. http://www.auto21.ca/ *Network of Centers of Excellence on the Automobile of the 21st Century.* Page web consulted 2003 Nov 09.
2. Edu Ruiz, Achim V., Soukane S., Trochu F., Breard J. Optimization of injection flow rate to minimize micro/macro-voids formation in resin transfer molded composites. *Composites Science and Technology.* 2005; doi:10.1016/j.compscitech.2005.06.013.
3. Edu Ruiz, Demaria C., *Diseno, Análisis y Procesos de Fabricación de la puerta de un vehículo eléctrico ciudadano en RTM.* Eng. repport, Instituto Universitario Aeronáutico, Univ. Católica de Cordoba, Argentine, 1998; 320 pgs.
4. Voller V., Peng S. An Algorithm for the Analysis of Polymer Filling Molds. *Polymer Eng. and Sci.* 1995; **35**(22):1758-1765.
5. Maier R., Rohaly T., Advani S. G., Fickie K. A Fast Numerical Method for Isothermal Resin Transfer Molding Filling. *Int. Journal for Numerical Methods in Eng.* 1996; **39**:1405-1417.
6. Achim V., Edu Ruiz, Soukane S., Trochu F. Optimization of Flow Rate in Resin Transfer Molding (RTM). *8th Japan International SAMPE Symposium and Exhibition* (*JISSE-8*) Tokyo, Nov. 18-21 2003.
7. Trochu F, Boudreault J. F., Gao D. M., Gauvin R. Three-Dimensional Flow Simulations for the Resin Transfer Molding Process. *Materials and Manufacturing Processes.* 1995; **10**(1):21-26.
8. Remacle J.-F., Breard J., Trochu F. A Natural Way to Simulate Flow Driven Injections in Liquid Composite Molding. *Proc. CADCOMP 98, Computer Methods in Composite Materials.* 1998; **6**:97-107.
9. Trochu F., Gauvin R., Gao D. M. Numerical Analysis of the Resin Transfer Molding Process by the Finite Element Method. *Advances in Polymer Technology.* 1993; **12**(4):329-342.

10. Bohr E. *Etude des Échanges Thermiques dans la Fabrication des Composites par les Procedés d'Injection sur Renfort.* Mémoire de Maîtrise en Sciences Appliquées. Dep. Génie Mécanique. Ecole Polytechnique de Montreal. 2000; 267 pgs.
11. PAM-RTM™ *User's Documentation.* ESI_Group Software manual. 2002.
12. QUICK-FORM™ *User's Documentation.* ESI_Group Software manual. 2002.
13. PAM-FORM™ *User's Documentation.* ESI_Group Software manual. 2002.
14. Diallo M. L., Gauvin R., Trochu F. Experimental Analysis and Simulation of Flow Through Multi-layer Fiber Reinforcements in Liquid Composite Molding. *Polymer Composites.*1998; **19**(3):246-256.
15. Bréard J., *Materiaux Composites à Matrice Polymère.* Phd. Thesis, Université du Havre, France, 1997; 195 pgs.
16. Hammami A., Gauvin R., Trochu F., Touret O., Ferland P. Analysis of the Edge Effect on Flow Patterns in Liquid Composite Molding. *Applied Composite Materials.* 1998; **5**:161-173.
17. Pillai K. M., Tucker C. L., Phelan F. R. Numerical simulation of injection/compression liquid composite molding. Part 1. Mesh generation. *Composites: Part A.* 2000; **31**:87–94.
18. Bréard J., Trochu F. *Modélisation de la Dynamique des Écouplements d'un Fluid Réactif à Travers un Milieu Poreux Déformable en Condition Anisotherme. Application : procédés LCM.* Internal report, Ecole Polytechnique de Montréal, 1999.